OXFORD

Cerebral Cortex, May 2022;32: 1055–1076

https://doi.org/10.1093/cercor/bhab266
Advance Access Publication Date: 26 August 2021
Original Article

ORIGINAL ARTICLE

Kv2.1 Potassium Channels Regulate Repetitive Burst Firing in Extratelencephalic Neocortical Pyramidal Neurons

Greg S. Newkirk[1], Dongxu Guan[2], Nikolai Dembrow[1,3], William E. Armstrong[2], Robert C. Foehring[2] and William J. Spain[1,3]

[1]Department of Physiology and Biophysics, University of Washington, Seattle, WA 98195, USA, [2]Department of Anatomy and Neurobiology, Neuroscience Institute, University of Tennessee Health Science Center, Memphis, TN 38163, USA and [3]Epilepsy Center of Excellence, Veterans Affairs Puget Sound Health Care System, Seattle, WA 98108, USA

Address correspondence to William J. Spain, Department of Physiology and Biophysics, University of Washington, 1705 N.E. Pacific St., Box 357290, Seattle, WA 98195, USA. Email: spain@uw.edu

Abstract

Coincidence detection and cortical rhythmicity are both greatly influenced by neurons' propensity to fire bursts of action potentials. In the neocortex, repetitive burst firing can also initiate abnormal neocortical rhythmicity (including epilepsy). Bursts are generated by inward currents that underlie a fast afterdepolarization ($_f$ADP) but less is known about outward currents that regulate bursting. We tested whether Kv2 channels regulate the $_f$ADP and burst firing in labeled layer 5 PNs from motor cortex of the *Thy1-h* mouse. Kv2 block with guangxitoxin-1E (GTx) converted single spike responses evoked by dendritic stimulation into multispike bursts riding on an enhanced $_f$ADP. Immunohistochemistry revealed that Thy1-h PNs expressed Kv2.1 (not Kv2.2) channels perisomatically (not in the dendrites). In somatic macropatches, GTx-sensitive current was the largest component of outward current with biophysical properties well-suited for regulating bursting. GTx drove ~40% of *Thy1* PNs stimulated with noisy somatic current steps to repetitive burst firing and shifted the maximal frequency-dependent gain. A network model showed that reduction of Kv2-like conductance in a small subset of neurons resulted in repetitive bursting and entrainment of the circuit to seizure-like rhythmic activity. Kv2 channels play a dominant role in regulating onset bursts and preventing repetitive bursting in *Thy1* PNs.

Key words: afterdepolarization, cortical rhythm, epilepsy, guangxitoxin, Thy1-h neuron

Introduction

Numerous studies suggest that there are two broad classes of pyramidal neurons (PNs) in neocortex, separated by their projection targets into those that project only within the telencephalon (intratelencephalic projecting: IT-type) and those that project beyond the telencephalon (pyramidal tract- or PT-type: Reiner et al. 2003, 2010; Anderson et al. 2010; Suter et al. 2013). We favor the more descriptive and inclusive term extrapyramidal (ET-type) for the latter, since not all areas of neocortex project within the pyramidal tract (Baker et al. 2018). Layer 2/3 PNs are IT-type. Layer 5 PNs include both IT- and ET-type (Reiner et al. 2003, 2010; Anderson et al. 2010; Dembrow et al. 2010; Groh et al. 2010; Suter et al. 2013; Guan et al. 2015). Besides differences in projections, numerous studies have shown that IT- versus ET-type PNs differ in morphology (Chagnac-Amitai et al. 1990; Mason and Larkman 1990; Agmon and Connors 1992; Tseng and Prince 1993), sublaminar localization (Mason and Larkman 1990; Reiner et al. 2003; Suter et al. 2013), synaptic inputs (de Kock et al. 2007; Brown and Hestrin 2009; Anderson et al. 2010; Suter et al. 2013), and physiological properties (Connors et al. 1982; McCormick et al. 1985; Mason and Larkman 1990; Hattox and Nelson 2007; Dembrow et al. 2010; Groh et al. 2010;

Suter et al. 2013; Guan et al. 2015). These PN subtypes have distinct functions: For example, anesthetics elicit burst firing in ET but not IT PNs (Christophe et al. 2005) and IT but not ET PNs mediate responses to antidepressants (Schmidt et al. 2012).

Early work from the Prince lab (Connors et al. 1982; McCormick et al. 1985) showed that while most neocortical PNs fired repetitively and regularly in response to a DC current injection, a subset of PNs in layers 4 and 5 responds to such stimuli with an initial burst of high-frequency action potentials (APs) riding on a slow depolarization, with a subsequent return to the regular spiking pattern. Despite differences between labs and species in the frequency of occurrence of such intrinsic burst firing neurons, depending upon recording conditions (e.g., internal anion, degree of chelation, temperature, extracellular K^+ or Ca^{2+} concentration, amount of dendrites or axon that survives the slicing procedure, DC vs. rapidly fluctuating inputs), there is general agreement that a subset of layer 5 PNs with somas in deep layer 5 and with prominent apical dendrites that extend all the way to the pia is the most likely to show onset burst firing (Mason and Larkman 1990; Larkman and Mason 1990; Tseng and Prince 1993; Larkum et al. 1999, 2004; Williams and Stuart 1999). These PNs correspond to ET-type PNs, although under the right conditions, virtually all PNs can fire with an onset burst (e.g., Larkum et al. 2007). ET-type PNs provide the main output from cortex and they project beyond the telencephalon (Reiner et al. 2003; Anderson et al. 2010; Dembrow et al. 2010; Reiner et al. 2010). Consistent with onset bursting being most common in ET-type PNs that provide cortical output and have long horizontal projections (Telfeian and Connors 1998), this cell type is implicated in the initiation and spread of seizure activity of neocortical origin (Connors 1984; Wong et al. 1986; Chagnac-Amitai and Connors 1989; Silva et al. 1991; Telfeian and Connors 2003; Pinto et al. 2005; Traub et al. 2005).

Two main mechanisms have been proposed to underlie onset burst firing in PNs. One model suggests that bursting occurs when back propagating Na^+ action potentials depolarize an apical dendritic site of Ca^{2+} electrogenesis, resulting in a dendritic Ca^{2+} AP that propagates to the soma, where it elicits a slow depolarization that summates with Na^+ currents at the axonal initial segment (AIS), resulting in a burst of Na^+ APs (Larkum et al. 1999, 2004; Williams and Stuart 1999; Oakley et al. 2001a, 2001b). Another model emphasizes the role of an intact axon for burst firing and proposed that the inward current underlying the burst comes from back propagation of axonal persistent Na^+ current to the soma (Guatteo et al. 1996; Debanne 2011; Kole 2011). These two mechanisms are not mutually exclusive.

Less is known about what controls these inward currents to regulate burst firing. In general, the filtering by potassium (K^+) channels of the transform from synaptic input to spike output shapes neuronal computation. Our previous work has identified many voltage- and Ca^{2+}-gated K^+ channels in neocortical PNs that could potentially regulate burst firing. These include Kv1, Kv2, Kv4, Kv7, SK, and $_s$AHP currents (Guan et al. 2006, 2013, 2015; Guan, Armstrong, et al. 2007a; Guan, Lee, et al. 2007b; Higgs and Spain 2009, 2011; Guan, Higgs, et al. 2011a; Guan, Horton, et al. 2011b; Bishop et al. 2015; see also: Schwindt et al. 1988; Lorenzon and Foehring 1992; Foehring and Surmeier 1993; Pineda et al. 1998, 1999; Bekkers 2000; Korngreen and Sakmann 2000; Abel et al. 2004; Norris and Nerbonne 2010). In particular, the perisomatic localization, large amplitude, moderately fast kinetics of activation, and slow inactivation of Kv2 currents suggest that these channels might be important in regulating burst firing (Murakoshi and Trimmer 1999; Guan, Armstrong, et al. 2007a; Guan et al. 2013; Liu and Bean 2014; Bishop et al. 2015). In addition, three recent studies have reported that pharmacological block of Kv2 channels in CA3 PNs, substantia nigra neurons, or entorhinal cortex stellate neurons resulted in some form of bursting to a limited set of inputs (e.g., large phasic stimuli in CA3, small tonic stimuli in stellate neurons; Kimm et al. 2015; Hönigsperger et al. 2017; Raus Balind et al. 2019).

In order to reliably target ET neurons in layer 5 of motor cortex, we studied the function of Kv2 channels in the *Thy1-h* mouse line (hereafter referred to as *Thy1* PNs: Feng et al. 2000), a genetically and physiologically distinct subset of ET PNs that express yellow-fluorescent protein (EYFP) in deep layer 5. *Thy1* PNs are large and have extratelencephalic (ET) projecting axons. Our main finding is that the dominant function of Kv2 channels in *Thy1* PNs is to regulate high-frequency bursts of action potentials. In addition, because burst firing is associated with rhythmic activity in neocortex (Rodriguez et al. 1999; Fries et al. 2001; Siegel et al. 2008; Womelsdorf et al. 2014; Sacchet et al. 2015) and mutations affecting Kv2 function are associated with (and likely cause) some forms of familial epilepsy (D'Adamo et al. 2013; Speca et al. 2014), we used our experimental results to model whether suppression of Kv2 channel activity in this subset of neurons could result in rhythmic oscillations in a local cortical circuit, which could in turn facilitate seizures.

Materials and Methods

All experiments were performed in accordance with institutional and national guidelines for animal care and were approved by the Institutional Animal Care and Use Committees at the University of Washington and the University of Tennessee Health Science Center.

Slice Preparation

Both female and male 4–8 weeks old mice from *Thy1* EYFP lines were anesthetized using either an intraperitoneal injection of ketamine (130 mg/kg)/xylazine (8.8 mg/kg) mixture or after exposure to isoflurane. Some mice were then perfused through the heart with ice-cold saline containing the following (in mM): 2.5 KCl, 1.25 NaH_2PO_4, 25 $NaHCO_3$, 0.5 $CaCl_2$, 7 $MgCl_2$, 7 dextrose, 205 sucrose, 0.4 to1.3 ascorbate, and 1 to 3 sodium pyruvate bubbled with 95% O_2/5% CO_2 (carbogen) to maintain the pH at 7.4 (others were not perfused). Brains were removed and a coronal blocking cut containing the motor cortex was attached to a vibrating tissue slicer (Leica, Germany or Vibroslice: Cambridge). The 300-μm-thick coronal sections were collected in ice-cold saline identical to perfusion solutions and subsequently stored in holding solution containing the following (in mM): 125 NaCl, 2.5 KCl, 1.25 NaH_2PO_4, 25 $NaHCO_3$, 2 $CaCl_2$, 2 $MgCl_2$, 12.5 dextrose, and 3 sodium pyruvate (bubbled with carbogen) at 35 °C for 30 min and then at room temperature.

Methods for Dissociated Cells

For details on cell dissociation procedures, solutions, and voltage protocols for isolation of the A-current, please refer to Guan, Higgs, et al. (2011a); Guan, Horton, et al. (2011b). In brief, 5–8 weeks old *Thy1* mice were used. The brain was removed after decapitation under isoflurane anesthesia and cut into 300-μm-thick coronal slices in ice-cold high sucrose solution. Area of motor cortex was further dissected from slices as to 1–2 mm^2 squared blocks. Four to six such cortical blocks were treated in

enzyme solution (Protease IV, 0.7 mg/mL in aCSF) at 34 °C for 35 min. After three rounds of gradually size-confining trituration, the supernatant of dissociated neurons was placed in a 35-mm petri dish and observed under Nikon inverted microscope (DIAPHOT 300).

External Solutions

Current-clamp external solutions contained the following (in mM): 125 NaCl, 3 KCl, 1.25 NaH_2PO_4, 26 $NaHCO_3$, 2 $CaCl_2$, 1 $MgCl_2$, 17 dextrose, 3 sodium pyruvate (bubbled with carbogen). In all experiments using only injected current stimuli, the aCSF also contained 6,7- dinitroquinoxaline-2,3-dione (DNQX, 20 μM), D-(−)-2-amino-5-phosphonopentanoic acid (D-AP5, 20 μM), picrotoxin (100 μM), and CGP66845 (2 μM) to block synaptic input mediated by AMPA/kainate, NMDA, $GABA_A$, and $GABA_B$ receptors, respectively (DNQX and D-AP5 were omitted in the experiments using 2p-glu stimulation). The Kv2 channel blocker Guangxytoxin-1E (GTx; Alomone Labs, Jerusalem, Israel) was bath applied at 100 nM together with 0.25% bovine serum albumin (BSA) (recirculating bath system with constant flow of ~2 mL/min). In experiments using the Kv4 channel blocker, AmmTx3 (200 nM, Smartox Biotechnology, Saint-Egrève, France) recording conditions were consistent with GTx application. Recordings were performed at 33–35 °C.

The external solution for outside-out macropatches contained the following (in mM): 125 NaCl, 3 KCl, 2 $CaCl_2$, 2 $MgCl_2$, 1.25 NaH_2PO_4, 26 $NaHCO_3$, and 20 glucose (pH 7.4, 310 mOsm; bubbled with carbogen). For dissociated cell experiments, a HEPES buffered solution was used that contained (in mM): 140 sodium isethionate, 3 KCl, 1 $MgCl_2$, 12 glucose, 10 HEPES, and 1.6 $CaCl_2$. To isolate potassium channels in voltage clamp (slice, macropatch, and dissociated cells), external solutions contained 1 μM tetrodotoxin (TTX; Tocris) and 100–400 μM $CdCl_2$ for blocking Na^+ and Ca^{2+} channels, respectively. Recordings were performed at 33–35 °C, except for dissociated cells (RT).

Internal Solutions

In current-clamp configuration, recording pipettes were filled with an internal solution containing (in mM): 140 K gluconate, 14 KCl, 10 HEPES, 4 Mg adenosine 5-triphosphate (ATP), 0.3 NaGTP, 7 2 K phosphocreatine, and 4 2Na phosphocreatine (pH 7.42 with KOH) and Neurobiotin (0.1–0.2%). Alexa 594 (40 μM) and Oregon Green BAPTA-6F (100 μM) were added for two-photon imaging and uncaging experiments (see below). The liquid junction potential (8–9 mV) was uncorrected for current-clamp experiments.

For macropatch experiments, electrodes were filled with an internal solution containing (in mM): 130.5 $KMeSO_4$, 10 KCl, 7.5 NaCl, 2 $MgCl_2$, 10 HEPES, 2 Na_2ATP, 0.2 guanosine 5-triphosphate (GTP: sodium salt), and 5 mM EGTA to prevent activation of Ca^{2+}-dependent conductances.

For dissociated cells, the internal solution consisted of (in mM): 86 $KMeSO_4$, 54 KOH, 2 $MgCl_2$, 40 HEPES, 2 Na_2ATP, 0.2 NaGTP, 9 creatine phosphate, 0.1 leupeptin, 10 BAPTA (pH 7.2; 270 mOsm). The liquid junction potential (8 mV) was corrected for voltage-clamp experiments.

Recordings

Layer 5 PNs in the motor cortex that expressed EYFP (*Thy1*) were targeted for somatic recording using epifluorescence combined with IR-DIC. Recordings were performed in current-clamp configuration from whole-cell patch pipettes made from borosilicate glass (Sutter, Novato, CA, USA) with tip openings of about 1 μm and resistances of 4–6 MΩ following coating of the taper with Sylgard to reduce capacitance. Recordings were performed using an Axopatch 2B or Multiclamp 2A amplifier (Molecular Devices, Sunnyvale, CA, USA) in bridge balance mode, either with 10 kHz low-pass filtering and 20 kHz data sampling through an ITC-18 digital board (HEKA, Holliston, MA, USA) and controlled using custom protocols written in Igor Pro (Wavemetrics, OR, USA) or using PClamp 9. Reported voltages were not corrected for the measured liquid junction potential (8–9 mV). Recordings with >25 MΩ series resistance or < 0 mV spike overshoot were discarded.

Voltage-clamp recordings were performed using an Axon Multiclamp 700A amplifier (Molecular Devices, Sunnyvale, CA, USA) and PClamp 9 software digitized at 10 kHz and filtered at 4 kHz. Some voltage-clamp experiments to test for selectivity of GTx or AmmTx were performed as whole-cell recordings in the slice preparation. This preparation allowed us to record from cell types identified by EGFP/YGFP. To allow accurate biophysical measurements of outward K^+ currents in dendritic neurons where space-clamp is a serious issue for whole-cell recording, we used outside-out macropatches for all of the detailed biophysics. These macropatches were obtained by forming a 1-GΩ or tighter seal and slowly withdrawing the pipette following break-in to whole-cell mode. Macropatch capacitance in this configuration was typically 2–4 pF and R_{series} was 5–9 MΩ. All reported voltages were corrected by subtracting the measured liquid junction potential (8 mV). For dissociated cell recordings, electrode resistances were 1.4–2.2 M. Series resistance was compensated by 70–90%. Cells with calculated series resistance errors of >5 mV were discarded (series resistance error = series resistance after compensation (G) multiplied by peak current (pA)).

Stimulation in Current-Clamp Experiments

Glutamate Uncaging

Precise focal activation of individual dendritic spines was performed using a two-photon laser-based scanning system from Bruker Technologies (Middleton, WI). Pulsed laser light (80 MHz; Chameleon Ultra II; Coherent; Santa Clara, CA) at 810 nm was guided by galvanometer-controlled (6 mm, Cambridge) mirrors through a 40× objective on a Zeiss microscope for imaging. Reflected fluorescent light was separated using two dichroic mirrors and through green (ET525/70 m-2P; Chroma) and red (ET650/75 m-2P; Chroma) emission filters and collected using gallium arsenide phosphide (GaAsP) detectors. The 2048 × 2048 pixel images were collected of the 300 × 300 μm (1×) or 75 × 75 μm (4×) field of view using PrairieView (v4.3.2.6) software. To photolyze caged glutamate, a second two-photon laser (Chameleon Ultra II; Coherent) at 720 nm was used and guided by a separate set of galvanometer-controlled (3 mm, Cambridge) mirrors into the light path. The intensity of each laser beam reaching the sample was independently attenuated using an electro-optical modulator (Pockels cell). In addition, the uncaging pathway passed through a homemade passive 8× pulse splitter to reduce photodamage (Ji et al. 2008). 4-Methoxy-7-nitroindolinyl-caged-L-glutamate (MNI-glu; Tocris, Bio-Techne, Minneapolis, MN) was bath applied at 4 mM and recirculated using an oxygenated reservoir (5 mL). PrarieView and TriggerSync (v2.0.5) software was utilized in conjunction

with custom-written acquisition code in MATLAB (R2012b; Mathworks, Natick, MA) to 1) control laser intensity, 2) control the galvanometer-controlled beam location within the field of view, and 3) to collect imaging, stimulation parameters and electrophysiological data. Spines that were within an optical depth (z-section) were targeted for focal caged glutamate photolysis adjacent to the spine head using 0.2 ms exposure times. Spines on a specific dendrite segment were stimulated in random order with a 0.3 ms interspine-stimulus interval.

Noisy Current Stimulation

We determined the effect of Kv2 channel blockade on neuron resonant firing properties during noisy somatic current injection. Noise stimulations consisted of a noisy current and a DC offset that was adjusted after each 10-s trial to maintain a targeted firing rate. The noisy portion of the current was set to have a standard deviation (SD) to give a 2 mV SD membrane potential (*Vm*) fluctuation when the neuron was held at a mean *Vm* of −70 mV (i.e., close to resting membrane potential: RMP) in control solution. The noise was created using an Ornstein–Uhlenbeck process as in Higgs and Spain (2011), and was filtered with a 5-ms time constant. For frequency-current curves, this noisy portion of current was added to DC steps. For gain–frequency analysis, the mean firing rate was then set to 20 Hz by adding DC current to the noise. The mean rate was maintained at 20 Hz after bath application of GTx by adjusting the DC current while maintaining the SD of the noise at its original setting. We collected 2000 spikes for analysis, by 10 repeats of 10-second trials of 20-Hz firing. The noise added to the traces was varied between trials, but frozen between control and GTx experiments.

Immunocytochemistry and Histology

Thy1 mice ($n = 4$, P26–P42) were anesthetized with sodium pentobarbital (50 mg/kg i.p.). The anesthetized animals were transcardially perfused with 0.01 m sodium phosphate buffer plus 0.89% NaCl (PBS) followed by PBS-buffered 4% paraformaldehyde and 0.2% picric acid. Brains were removed, postfixed for ~12 h at 4 °C, then blocked, and placed in a solution of fixative containing sucrose (30% w/v) for cryoprotection. Sections through the cortex were taken at 50 μm on a freezing microtome (VT1000 Leica, Bannockburn, IL, USA), rinsed several times in PBS containing 0.5% Triton X-100 (PBST), and incubated in 10% normal goat serum for 1 h to block nonspecific binding. The sections were subsequently incubated in NeuroMab monoclonal antibodies to Kv2.1 (K89/34; 10 μg/mL; NeuroMab #73-014) and Kv2.2 (N372B/1: NeuroMab #73-369; N372B/60: NeuroMab #73-360; N372C/51: NeuroMab #73-358). After three rinses in PBST, the sections were incubated in the secondary antibody: Alexa Fluor 568-conjugated goat antimouse IgG1 (1:200, Vector Labs) for 4 h at room temperature. The sections were rinsed several times in PBST, mounted on a glass slide, and cover-slipped with polyvinyl alcohol (PVA) solution containing 6 g/25 mL glycerol, 2.4 g/25 mL PVA, 0.625 g/25 mL of the antifade reagent 1,4 diazabicyclo[2.2.2]octane, brought to 25 mL with 6 mL dH_2O, and 12 mL PBS (all reagents, Sigma-Aldrich, St Louis, MO, USA). These sections were viewed with a Zeiss 710 confocal microscope (Carl Zeiss, Oberkochen, Germany). Positive transgenic EYFP neurons were examined with a laser excitation wavelength of 488 nm, whereas neurons immunostained for Kv2.1 or Kv2.2 with Alexa Fluor 568-labeled secondary antibody were examined with a 568-nm laser line. The optical section thickness was 2 μm. Sections were viewed singly or in stack sections using ×20 (NA 0.8) or ×40 oil immersion objectives (NA 1.3). Confocal images (1024 × 1024 pixels) were viewed with Zen (Carl Zeiss) or ImageJ (NIH) software. The final confocal figures were made in Adobe Illustrator, with minimal alteration in dynamic range.

Slice recordings contained Neurobiotin in the internal solution for preservation of cell localization and structure using a diaminobenzidine (DAB)-based processing (described in detail in Marx et al. 2012). Following withdrawal of the pipette after recordings, slices were transferred to 3% glutaraldehyde in phosphate buffer (PB) and stored at 4 °C for several days. The cells were then incubated in 0.5% Triton-X PB and 1% hydrogen peroxide for 3 h, followed by an overnight incubation in Avidin-DH and Biotinylated horseradish peroxidase. The slices were then incubated for 1 h in the DAB stock, which was oxidized by dilutions of 3% hydrogen peroxide in water. The slices are mounted on slides for light microscopy with a Eukitt (Sigma-Aldrich, St. Louis, MO) embedding. Kole (2011) has shown that a longer preserved axon in layer 5 PNs studied in vitro was associated with burst firing occurring. We tested if a longer axon length was related to the likelihood of repetitive bursting after Kv2 channel block during the noisy current injections in the 17 neurons included in Figure 8. Neurobiotin fills were obtained for 14 of the 17 neurons and we measured the axon length that was clearly traceable (axon length measurements were not corrected for tissue shrinkage). The mean axon length ± SD was 154 ± 181 μm in the group without repetitive bursting ($n = 7$) compared with 64 ± 37 μm in the repetitive bursting group ($n = 7$), $P = 0.22$ (two-tailed students *t*-test). For neurons tested with DC current steps, we recovered neurobiotin fills in 34 neurons. The mean ± SD axon length was 92 ± 62 μm in 23 neurons that had only an initial burst (in GTx) and was 93 + 87 μm in 11 neurons that had repetitive bursting (nsd; $P = 0.97$, two-tailed students *t*-test).

Analysis

Analysis of Voltage Clamp (Outside-Out Macropatch) Experiments

Data were obtained at 10 kHz and filtered at 4 kHz. To determine steady-state voltage-dependence, a family of 500 ms voltage steps were made from a holding potential of −80 mV to voltages between −50 and +50 mV in 20 mV increments (20s between sweeps). This protocol was run in control solution and repeated after application of 100 nM GTx. The GTx-sensitive current was obtained by subtracting traces in GTx from control traces. Current at 500 ms was converted to conductance by dividing current by driving force ($E\text{-}E_{K+}$; E_{K+} was calculated as −102 mV from the internal and external K^+ concentrations). Conductances were normalized by the maximum conductance and the normalized conductance was plotted as a function of test voltage. These data were fit with a single Boltzmann relationship (equation (1)).

$$G = \frac{G\,\max}{1 + \exp\left(\frac{Vh - V}{Vslope}\right)} \quad (1)$$

where *G* is the calculated conductance, G_{max} is the maximal conductance, *V* is the step potential, V_h is the half-activation or half-inactivation voltage, and V_{slope} is the slope. Data were well fit by a single Boltzmann equation.

To determine activation and inactivation kinetics, we fit the rising phase and decay phase of currents, each with a single exponential (first order: equation (2)). A 500-ms step from −75 to 0 mV was used (20 s between steps). GTx-sensitive

currents without a readily observable A-current component (identified as a fast peak in the first 2 ms after step onset in a few recordings) were used to fit the following activation–inactivation equation:

$$I(t) = I_o\left(1 - \exp\left(-\frac{t}{\tau_o}\right)\right)\exp\left(-\frac{t}{\tau_1}\right) \quad (2)$$

where $I(t)$ represents the GTx-sensitive current, τ_0 is the activation time constant, and τ_1 is the inactivation time constant.

Spike Detection and Threshold

Current-clamp recordings were digitized and action potentials were detected when the spike overshoot was greater than 0 mV. Spike threshold was calculated by giving the cell a series of identical pulses where the current elicited an action potential on approximately 50% of the trials. Trials that did not induce an action potential were averaged and the voltage level at the end of the trajectory was collected and reported. We found this to be a more consistent and precise measurement of threshold compared with the dV/dt > 20 mV/ms that we used for spike timing.

Normalization of Interspike Interval Histograms

The interspike interval histograms in Figures 7C and 6E,F were all performed the same way. The interspike interval was calculated from the time difference in measured threshold (the point where dV/dt > 20 mV/ms) between spikes. The interspike intervals for a given cell was plotted with a bin size of 0.5 ms and a maximum bin of 150 ms. Each cell was then normalized by dividing the histogram by the number of total spikes analyzed for that cell to convert spike count to "percentage of total spikes." We then were able to average histograms across cells and apply statistics to the results.

STA Analysis

The spike-triggered average (STA) was calculated using the following: For n spikes, I_{STA} was calculated as the mean I_{noise} at a time delay τ with respect to each spike time, t:

$$I_{STA}(\tau) = \frac{1}{n}\sum_{s=1}^{n} I_{noise}(t - t_s) \quad (3)$$

Gain–Frequency Analysis

The frequency-dependence of the gain was quantified by correlation analysis of responses to noisy current where the target firing rate was set to 20 Hz and adjusted by DC input. The stimulus–response correlation and stimulus autocorrelation were combined with time differences and stimulus to obtain Fourier components that were used to calculate the frequency-dependent gain as described in depth in Higgs and Spain (2009). The gain–frequency plot shows the relative efficacy of each frequency component of the noisy current input to modulating firing rate and as such it is a measure of suprathreshold resonance. Note that the gain–frequency analysis provides the local linear response for a given firing rate and set of noise statistics (e.g., time constant, SD). Any change in those variables can (and does) cause some shift of the neurons' resonant firing properties (Higgs and Spain 2009).

Spectral Analysis of In Silico Neuron Network

To analyze the spectral components of the collective network output, all of the spike times were collapsed into a single train and convolved with a Gaussian function with an SD of 10 ms to generate an instantaneous network firing rate. From this estimate of the network firing rate, we performed a fast Fourier analysis and calculated the power density spectrum as the square of the frequency components.

Table 1 Parameter settings for the model neurons.

LIF neuron parameters	*E*	*I*
Membrane capacitance, C_m	500 pF	400 pF
Leak conductance, g_{Leak}	20 nS	15 nS
Initial V_m	−70 mV	−80 mV
Spike threshold, $V_{threshold}$	−55 mV	−56 mV
Postspike reset potential, V_{reset}	−60 mV	−60 mV
Absolute refractory period	2 ms	2 ms
$_f$ADP conductance increment, Δg_{fADP}	18 nS/spike	n/a
$_f$ADP decay time constant, τ_{fADP}	1.4 ms	n/a
$_f$ADP reversal potential, E_{fADP}	70 mV	n/a
$_m$AHP conductance increment, Δg_{mAHP}	9 nS/spike	n/a
$_m$AHP decay time constant, τ_{AHP}	50 ms	n/a
$_m$AHP reversal potential, E_{mAHP}	−100 mV	n/a
Kv2 conductance increment, Δg_{Kv2}	{0, 30} nS/spike	n/a
Kv2 decay time constant, τ_{Kv2}	5 ms	n/a
Kv2 reversal potential, E_{Kv2}	−100 mV	n/a

Statistics

Prism (GraphPad Software, San Diego, CA) software was used to perform statistical tests on the data obtained from the PNs. For CV measurements, a one-way randomized block ANOVA (experiments were treated as matched sets to account for experiment-to-experiment variability) with post-hoc Tukey's multiple comparisons test was used to determine which individual CV means differed, and summary data are presented as across-replicate means ± SEM. Paired *t*-tests were used to compare control versus drug effects. For all tests, *P* values <0.05 were considered to be significantly different. Sample population data and error bars in plots are represented as mean ± SEM unless otherwise specified.

The In Silico Simplified Neuron Network

Simulations were performed using MATLAB (Mathworks, Nattick, MA), with each voltage integration calculated by first-order Euler integration with a time increment of 0.05 ms.

The network model contained interconnected excitatory (*E*) and inhibitory (*I*) neurons. For *E* neurons, we used a single-compartment, leaky integrate-and-fire (LIF) neuron with conductances (g) for the $_f$ADP, $_m$AHP, and a Kv2-like conductance designed to capture experimentally measured features of *Thy1* neuron-firing properties under normal conditions and after block of Kv2 channels with GTx. The *I* neurons were single-compartment LIF neurons without added conductances. The parameters for the *E* and *I* neurons are shown in Table 1 (for *E* neurons in GTx, g_{Kv2} was set to zero and the post-AP reset was −58 mV instead of −60 mV).

When V_m was negative to $V_{threshold}$, the model behaved according to the following (see Table 1 for the *E* and *I* LIF neuron parameters):

$$dV_m/dt = (I_{stimulus} - I_m)/C_m \quad (4)$$

where V_m is membrane voltage, t is time, C_m is membrane capacitance, and I_m is membrane current.

$$I_m = g_{leak}(V_m - E_{leak}) + g_{fADP}(V_m - E_{fADP}) + g_{mAHP}(V_m - E_{mAHP}) + g_{kv2}(V_m - E_{kv2}) + g_{Etotalsyn}(V_m - E_{Esyn}) + g_{Itotalsyn}(V_m - E_{Isyn}) \quad (5)$$

and

$$I_{stimulus}(t) = I_{noise}(t) + I_{offset}(t) \quad (6)$$

where I_{offset} was the level of DC current and the noisy current component, I_{noise}, was created by convolving pseudorandom points chosen from a Gaussian distribution from −1 to 1 for each time interval, t, with an exponential filter, $\exp(-t/\tau)$, where $\tau = 3$ ms for inhibitory neurons and $\tau = 5$ ms in excitatory neurons. This pseudorandom series was multiplied by a specified amount of current to get the desired SD (the DC level and SD of the noise are specified for each experiment in results).

To generate a randomly connected network, pseudorandom numbers between 0 and 1 were selected for every connection (regardless of type). Any random number greater than the probability of connection was made zero (unconnected). Subsequently, all autapses were removed. Random connections between neurons were set to 10% of the total possible, with autapses removed (e.g., a network of 100 neurons had ∼1000 connections out of a possible 9900).

Individual excitatory and inhibitory synaptic conductances (g_{Esyn} and g_{Isyn}) were each calculated as the sum of two exponentials (fast rise and slow decay):

$$g_{syn}(t) = g_{Synmax} f \left(e^{-\frac{t-t_0}{\tau_{decay}}} - e^{-\frac{t-t_0}{\tau_{rise}}} \right) \quad (7)$$

where g_{syn} was the conductance of g_{Esyn} or g_{Isyn}; g_{Synmax} was their maximum conductance, which was set to 4 nS for both; τ_{rise} and τ_{decay} were rise and decay time constants: $\tau_{rise} = 0.2$ ms and $\tau_{decay} = 2$ ms for excitatory conductances and $\tau_{rise} = 0.5$ ms and $\tau_{decay} = 5$ ms for inhibitory conductances. To ensure the amplitude equaled g_{Synmax}, a normalization factor for the amplitude f was included, which was the inverse of the sum of the two exponentials at the peak of their sum in time. The start time for each conductance t_0 was set by a synaptic delay of 1.5 ms after the presynaptic spike. Reversal potentials for these conductances were $E_{Esyn} = 0$ mV and $E_{Isyn} = -70$ mV.

For every neuron, the total excitatory synaptic conductance ($g_{Etotalsyn}$) was the summed value of each of the individual excitatory synaptic conductances (g_{Esyn}) impinging onto that neuron at that time step and the total inhibitory synaptic conductance ($g_{Itotalsyn}$) was the sum of the individual inhibitory synaptic conductances (g_{Isyn}). The resultant synaptic currents were added with the other membrane currents to make I_m (as in equation (5)), which was in turn summed with the "external" current ($I_{stimulus}$).

After reaching $V_{threshold}$, V_m was set to V_{reset} for an absolute refractory period of 2 ms. Whenever threshold was reached, g_{fADP}, g_{mAHP}, and g_{Kv2} were increased at the next time point by the Δg amounts and decayed on subsequent time steps with the time constants listed in Table 1.

Results

Guangxitoxin-1E (GTx) Causes Action Potential Bursting in *Thy1* Neurons

We focused on identifying the potassium conductance that regulates the occurrence of burst firing in ET-type PNs. We concentrated our studies on *Thy1* PNs in acute brain slices from motor cortex because that region contains a particularly high density of L5-ET neurons. In initial experiments, we measured membrane voltage responses under conditions designed to mimic synaptic input onto the spines of the *Thy1* proximal dendrites using two-photon glutamate (2p-glu) uncaging. Somatically recorded postsynaptic potentials evoked by 2p-glu at individual spines had an average amplitude of 0.3 ± 0.02 mV and a half duration of 14.1 ± 1.0 ms ($n = 4$ cells and 113 spines). Stimulating a group of 21 to 31 nearby spines on one dendrite nearly simultaneously (Fig. 1A,B) evoked a large EPSP (7.3 ± 2.0 mV measured at the soma, $n = 4$; Fig. 1E). When this dendritic stimulation was combined with somatic DC current injection to depolarize the membrane potential, one or two APs were triggered, followed by a fast afterdepolarization ($_f$ADP) that decayed over ∼15 ms. We hypothesized that Kv2 channels might play a key role in shaping how dendritically evoked events are integrated in *Thy1* PNs.

To study the filtering effects of Kv2 channels on the 2p-glu evoked responses we used the selective Kv2 channel blocker GTx (Herrington et al. 2006; Liu and Bean 2014; Bishop et al. 2015; Hönigsperger et al. 2017; Pathak et al. 2016). Extracellular bath perfusion with GTx (100 nM) enhanced the $_f$ADP amplitude and increased the number of short-interval APs (i.e., a burst of spikes, as in Fig. 1C) driven by the dendritic stimulation. These data suggest that current through Kv2 channels dampens the $_f$ADP in *Thy1* PNs and limits bursting. When the holding current was reduced to allow baseline membrane potential to return to resting membrane potential (RMP), 2p-glu uncaging resulted in a subthreshold EPSP that was unaffected by GTx (Fig. 1E). Additionally, GTx had the same effect on supra- and subthreshold voltage responses in response to injection of an alpha function–shaped depolarizing current at the soma (Fig. 1D,F). Combined, these data suggest that Kv2 is minimally active at subthreshold voltages in the absence of spiking. Further, these data suggest that the Kv2 channels are located near the soma and exert their effects on the 2p-glu-induced depolarization at or near the soma, rather than locally in the dendrites. We set out to test these suggestions.

Functional Kv2.1 Channels Are Expressed on the Soma and Proximal Dendrites of Thy1 PNs

Previous work by our lab and others have shown that Kv2 channels have a perisomatic localization in PNs, including soma, proximal dendrites, and the AIS (Trimmer 1991; Misonou et al. 2005; Guan, Armstrong, et al. 2007a; Guan et al. 2013; Sarmiere et al. 2008; Bishop et al. 2015), but the distribution of Kv2 channels in *Thy1* PNs in the motor cortex had not been characterized. The Bishop et al. (2015) study showed that Kv2.1 channels were present on the soma and proximal dendrites (∼first 50 μm) of both IT-type (*etv1*) and ET-type PNs (*glt25*). In contrast, Kv2.2 channels were expressed in the same subcellular locations in *etv1* PNs but were not found in *glt25* PNs. Based upon this work, we hypothesized that the ET-type *Thy1* PNs would show a similar expression pattern to *glt25* PNs: that is, no Kv2.2 expression and perisomatic Kv2.1 expression. We tested this hypothesis

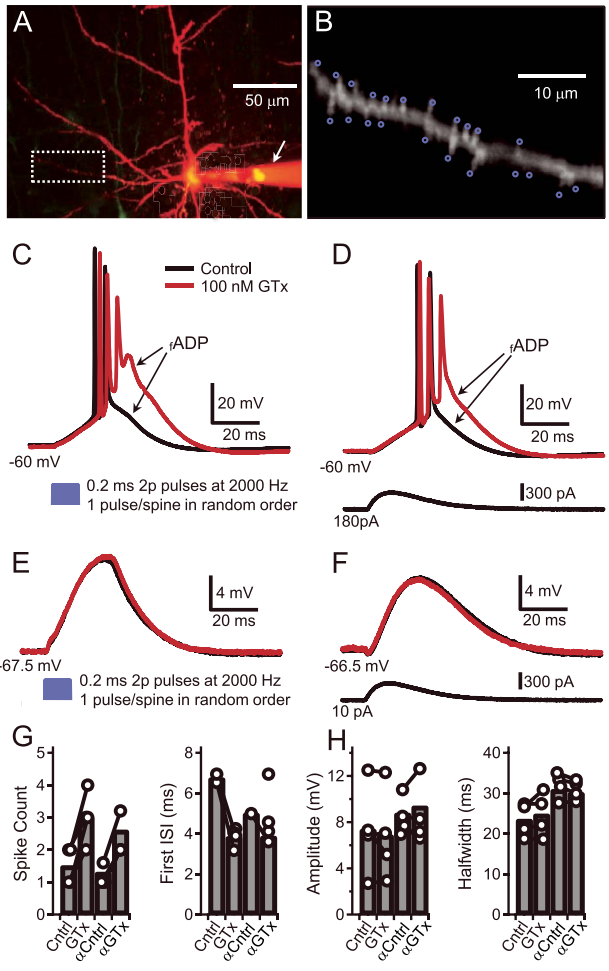

Figure 1. Block of Kv2 by GTx induces burst firing in *Thy1* PNs. (*A*) Composite maximum projection from a Z-stack of two-photon images of a *Thy1* PN in layer V of motor cortex filled with Alexa 594 (20 uM). The arrow indicates the Alexa containing microelectrode that was used for somatic current injection. Background florescence has been digitally reduced. (*B*) Magnification of the basal dendrite shown in *A* (white box) with blue circles to indicate the target areas adjacent to individual spines that were used to photolyze MNI-glu (bath applied, 4 mM; see Materials and Methods). (*C*) Voltage traces show suprathreshold dendritic branch activation after photolysis of MNI-Glu. The soma was depolarized to −60 mV via positive somatic current injection and glutamate was uncaged at each of the 19 foci indicated in *B* in random order (blue trace: the 2P laser light was on for 0.2 ms at each spine, wavelength, 720 nm; the repositioning interval, light off, was 0.3 ms). The somatically recorded voltage responses are shown before (black trace) and during bath application of GTx 100 nM (red trace). (*D*) Suprathreshold voltage responses before and during GTx in response to somatic injection of an alpha-EPSP waveform during somatic depolarization to −60 mV. (*E*) Subthreshold membrane voltage responses (at RMP) before and during GTx to 2P-uncaged glutamate (as in *C*). (*F*) Subthreshold voltage responses evoked by an alpha-wave current injection (near RMP). (*G*) Plots of spike count (left), and first ISI (right) for suprathreshold responses before (Cntrl) and during GTx to uncaged glutamate and to an alpha-wave (αCntrl, αGTx). Connected circles indicate values from the same cell; bars indicate mean of four cells. (*H*) Plots for subthreshold voltage response amplitudes (left) and half-widths of the same four cells in *G*.

on *Thy1* PNs by immunocytochemistry (Fig. 2*A*,*B*). Briefly, Kv2.1 and Kv2.2 expression was characterized using the K89/34 (for Kv2.1) and N372B/1 or N372B/60 (for Kv2.2) antibodies (both from NeuroMab) in 4 *Thy1* mice (P26–P42) (see Materials and Methods). Consistent with previous work on neocortical PNs, we found that Kv2.1 subunits were ubiquitously expressed in clusters on the membrane of the soma, AIS (Sarmiere et al. 2008), and proximal apical and basal dendrites (first 50–100 μm) of *Thy1* (EYFP-positive) and EYFP-negative PNs throughout layer 5 (and also ~all PNs in the other layers). We observed Kv2.1 expression in the proximal dendrites (apical and basal) and in the AIS, but as shown before (Trimmer 1991; Bishop et al. 2015), there was little evidence for expression in distal dendrites. Kv2.2 expression was nearly absent on the *Thy1* neurons, although it was clearly expressed in EYFP-negative PNs in layer 5. These data show that *Thy1* PNs express Kv2.1 in perisomatic compartments and generally do not express Kv2.2 channels (similar to *glt25* PNs). The dominant somatic location strategically places Kv2.1 channels for regulating the effects of inward currents reaching the soma from either the dendrites or the AIS.

Kv2 channels are one of several potassium channels that contribute to the sustained outward current in pyramidal neurons in response to long-lasting depolarization. We next used outside-out macropatch voltage clamp (VC) recordings pulled from the somas of *Thy1* PNs (capacitance of ~2–4 pF; see Bishop et al. 2015) to test for functional expression of Kv2 channel current and to determine its biophysical properties.

We first examined the affinity and selectivity of GTx for Kv2 channels in PNs. Preliminary experiments in acutely dissociated *Thy1* PNs revealed that the EC_{50} for GTx was ~14 nM ($n = 4$ cells, data not shown). We then examined selectivity in macropatches, using 0.5–1 s steps from a holding potential of −70 mV to a test potential of +10 mV (Fig. 2*C*). Not all somatic macropatches exhibited an obvious fast, transient "A-type" component to the current, consistent with the underlying Kv4 channels being in much higher density in the dendrites and the fact that the macropatches do not include the entire somatic membrane. In 11 macropatches that did have a clear initial A-type peak current followed by steady-state current (Fig. 2*F*), we found that 100 nM GTx blocked 65.6 ± 7.8% of the steady-state current (measured at 500 ms) but only 12.2 ± 3.8% of the peak current (or 6.6 ± 2.9% of A-type current, defined as peak–steady state). In 20 macropatches without a clear "A" component, GTx blocked 53.3 ± 4.1% of the steady-state current versus 58.8 ± 4.9% of the peak current. Collectively, these data suggest that 100 nM GTx blocks most of the putative Kv2-mediated current but only ~6% of transient, A-type current. Thus, GTx is selective for the sustained K^+ current (putative Kv2 current; see also Liu and Bean 2014; Bishop et al. 2015; Hönigsperger et al. 2017), comprising ~55% of total slowly inactivating K^+ current (Fig. 2*C*,*D*). The average Kv2 current amplitude in the macropatches was 216.3 ± 34.3 pA at the peak and 74.8 ± 16.3 pA at 500 ms ($n = 20$ patches; Fig. 2*D*). Our data show that Kv2 currents are the largest component of the sustained Kv currents in *Thy1* PNs.

AmmTx3 has been shown to selectively block Kv4 channels in association with dipeptidyl peptidase–like proteins (Maffie et al. 2013) and we previously found it to be selective for the A-type current in two other layer 5 PN subtypes, *etv1* and *glt25* (Pathak et al. 2016). As a further test of selectivity of GTx for Kv2 versus Kv4 channels, we used whole-cell voltage clamp in brain slices to compare current blocked by 100 nM GTx to that blocked by 400 nM AmmTx3. We used a protocol designed to isolate Kv4 current by subtraction (Supplementary Fig. 1). With a test step to −30 mV (a potential where it is easier to separate A-type vs. sustained K^+ current), GTx blocked 31 ± 6% of the steady-state current (at 500 ms) but only 3.7 ± 3.4% of the early peak "A" current ($n = 4$ cells). In contrast, AmmTx3 blocked 54.3 ± 7.6% of the early peak A current versus 0.4 ± 0.8% of the steady-state current. Thus, GTx is selective for the largest component of the

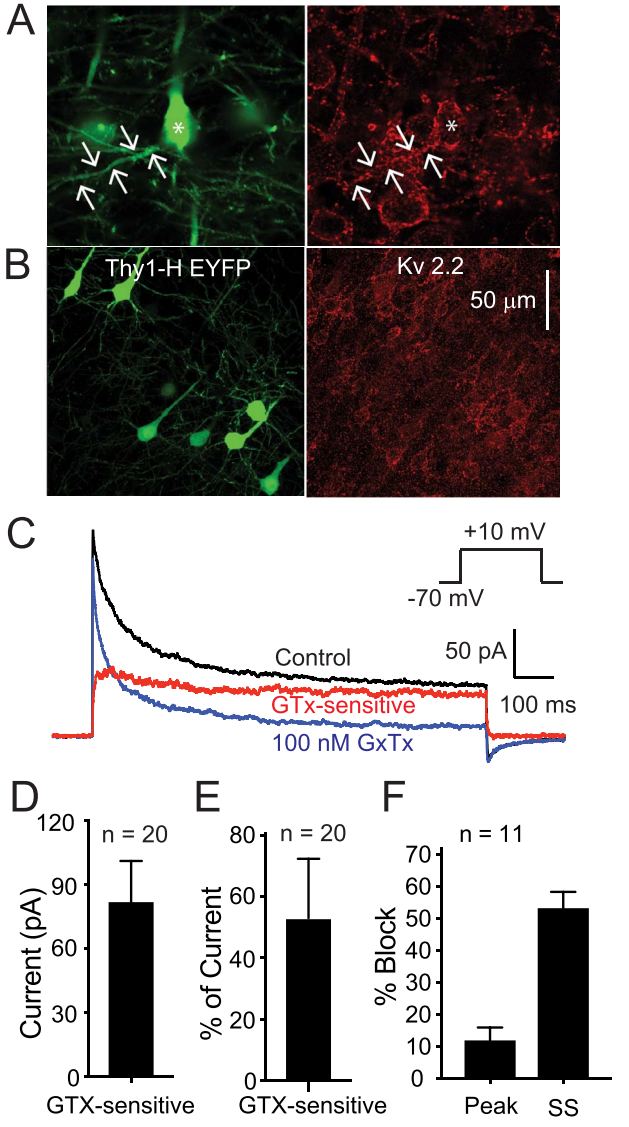

Figure 2. Kv2 channel expression on *Thy1* PNs in neocortex. (*A*) Photomicrographs showing *Thy1* (*EYFP* positive) L5 PNs from motor cortex (left panel) and immunocytochemistry for Kv2.1 (Neuromab K89/34: right panel). Scale bar applies to both images. Arrows indicate a basal dendrite. Note Kv2.1 is expressed on all PNs (*EYFP* positive and *EYFP* negative) on the soma and first 50–100 μm of the apical and basal dendrites. (*B*) Similar images showing EYFP (to indicate *Thy1* PN: left) and immunostaining for Kv2.2 (Neuromab N372B/1: right). Note that there is very little Kv2.2 expression on the EYFP-positive (green) PNs. Most of the Kv2.2 staining is on EYFP-negative (non-*Thy1*) PNs. (*C*) Current traces obtained from an outside-out macropatch from the soma of a *Thy1* PN from layer 5 of motor cortex (voltage protocol in inset). The black trace is in control solution, the blue trace is in the presence of 100 nM GTx), and the red trace is the GTx-sensitive current. In this cell, there is a clear fast transient component to the current in control solution (black). 100 nM GTx (blue) blocks a large percentage of the sustained current with only a small effect on the fast, transient current. (*D*, *E*) Summary data for voltage-clamp data from 20 macropatches that did not have an obvious "A" current component (from 20 *Thy1* PNs). (*D*) Summary data for 20 macropatches for absolute current blocked by 100 nM GTx. (*E*) Summary data for percentage of the current that was GTx-sensitive (measured at 500 ms). (*F*) Summary data for percentage of peak current versus steady-state current (SS: at 500 ms) blocked by 100 nM GTx in 11 macropatches with a clear transient "A" component to the control current (see text for further explanation).

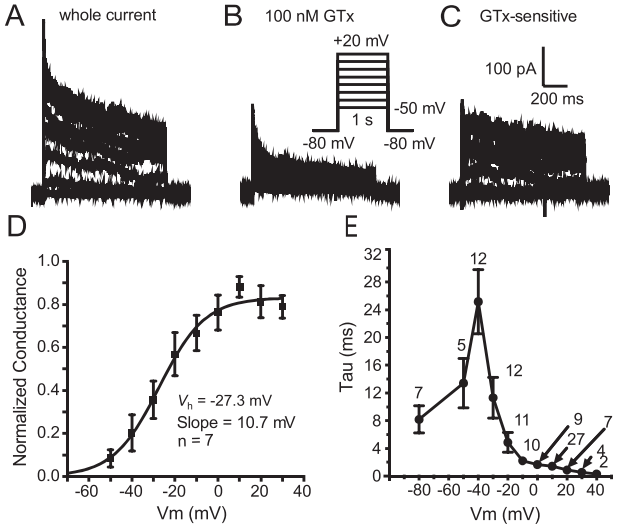

Figure 3. Characteristics of Kv2 current in *Thy1* neurons. (*A*) Example traces from a somatic outside-out macropatch in control solution (voltage protocol in inset in *B*). (*B*) Traces from the same macropatch during application of 100 nM GTx. (*C*) The GTx-sensitive current was obtained by subtraction. It activated relatively rapidly and inactivated slowly. (*D*) Summary activation voltage-dependence data for seven macropatches (mean ± SEM). The half-activation voltage ($V_{0.5}$) and slope are indicated on the graph. (*E*) Summary data for time constant (Tau) for activation and deactivation as a function of voltage (Data include 7 macropatches where we stepped to all voltages, as in *D*. At +10 mV, we had an additional 20 patches so $n = 27$). We fit the rising phase of the GTx-sensitive traces to obtain the time constants from above −50 mV, and we fit to the tail currents from the +10 mV step to voltages below −30 mV.

sustained current and AmmTx3 is selective for A-type current in *Thy1* PNs.

Characteristics of Kv2 Currents from *Thy1* Somas

We next used outside-out macropatches from *Thy1* PN somas and standard activation and inactivation VC protocols (see Materials and Methods) to determine steady-state activation and inactivation properties for the GTx-sensitive current. Previous work has found that in many PN types, Kv2 channels activate at relatively depolarized potentials compared with Kv1 or Kv7 (Murakoshi and Trimmer 1999; Guan,, Armstrong, et al. 2007a; Guan et al. 2013; Liu and Bean 2014; Bishop et al. 2015). In IT-type *etv1* PNs however, both Kv2.1 and Kv2.2 are expressed and the presence of Kv2.2 shifts activation to more negative potentials (including subthreshold voltages: Bishop et al. 2015). In contrast, in ET-type *glt25* PNs, only Kv2.1 is expressed and the voltage range for activation is more depolarized. We therefore hypothesized that the ET-type *Thy1* PNs would have a positive activation range for Kv2 current, since only Kv2.1 is expressed in these cells (Fig. 2A,B).

We tested activation kinetics and voltage-dependence with a family of 1 s steps to various potentials between −50 and +20 mV (10 mV increment). Putative Kv2-mediated current was isolated by subtraction of records in 100 nM GTx from control currents (Fig. 3A–C). Figure 3D shows an average steady-state activation curve obtained from 7 cells. In contrast to our hypothesis, the

GTx-sensitive current in *Thy1* PNs activates at relatively negative potentials, with an average half-activation voltage ($V_{0.5}$) of −27.3 mV and slope of 10.7 mV (Fig. 3D). Despite the absence of Kv2.2 channels, this is similar to activation of Kv2 in *etv1* PNs but negative to that in *glt25* PNS (Bishop et al. 2015). Figure 3E shows the voltage dependence of the activation time constant, τ, measured by fitting the rising phase of the current at various test potentials (exception: the −80 mV point is the deactivation τ at the holding potential). Figure 3E includes the data obtained at +10 mV for the seven cells tested at multiple potentials to determine the steady-state activation curve (Fig. 3A–D) plus 20 macropatches tested at +10 mV only. For the 20 macropatches tested with a single step to +10 mV, the τ was well fit with a single exponential with activation $\tau = 1.45 \pm 0.22$ ms and deactivation $\tau = 8.4 \pm 1.8$ ms (at −80 mV). Thus, these currents activate moderately rapidly and at subthreshold potentials and could influence AP threshold and postspike potentials (although they may activate too slowly to greatly influence AP properties: e.g., Pathak et al. 2016).

We also studied steady-state inactivation using outside-out macropatches from *Thy1* PN somas. The macropatches were held at −80 mV and then stepped to various potentials for 5 s before a test step to +10 mV (for 1 s) (Fig. 4). Currents were obtained before and during bath application of 100 nM GTx and the GTx-sensitive current obtained by subtraction (Fig. 4A–C). The currents were normalized to the largest current and plotted as a function of prepulse voltage (Fig. 4D). The data were well fit by a single Boltzmann equation (see Materials and Methods) with a half inactivation voltage (V_h) of −72.2 mV and slope of 14.9 mV ($n = 6$ macropatches; Fig. 4D,E). This is a fairly hyperpolarized inactivation V_h (e.g., more negative than Kv1 currents in layer 5 PNs: Guan et al. 2018). The kinetics of inactivation were obtained by fitting the decay of currents elicited by the activation protocol (Fig. 3) and are relatively slow ($n = 6$ macropatches; Fig. 4F). At +10 mV, the inactivation $\tau = 148.3 \pm 25.3$ ms. The slow inactivation and deactivation of Kv2 channels would facilitate regulation of afterpotentials and repetitive firing.

In summary, the properties of Kv2 channels are well suited to shape how *Thy1* PNs respond to strong synaptic activity. Based on their perisomatic location and the fact that they are the largest sustained K^+ current, Kv2 channels would be expected to filter the summed synaptic input from all dendrites. Based on the biophysical properties, a substantial amount of Kv2 conductance would be activated during spiking and could contribute to postspike membrane potential trajectories that control onset bursts and repetitive burst firing, depending on its contribution relative to other conductance mechanisms.

Kv2 Conductance Raises AP Threshold and Dampens the $_f$ADP

We next tested the effect of blocking Kv2 channels on AP firing evoked by various somatically injected current waveforms. All experiments employed whole-cell current-clamp and measurement of the membrane voltage output before and during application of GTx. Consistent with the voltage dependence of Kv2 channels in the macropatch experiments, GTx had no significant effect on the subthreshold current versus voltage relationship with current pulses of up to 1-s duration (steady-state input resistance for 43 cells in control: 37.1 ± 2.2 MΩ; GTx: 35.3 ± 2.5 MΩ).

To study the effects of Kv2 conductance on the transform of somatic current into AP firing, we used brief current pulses

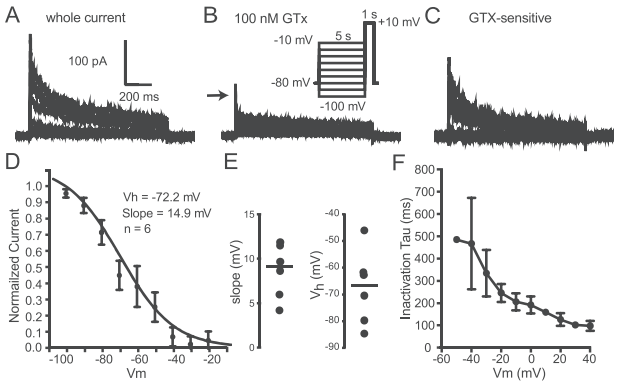

Figure 4. Steady-state inactivation. (*A*) Representative current traces from an outside-out macropatch in control solution in response to voltage protocol shown as inset in *B*. (*B*) Traces from the same macropatch in the presence of 100 nM GTx. Inset: voltage protocol for *A*–*C*. (*C*) GTx-sensitive currents for same macropatch as *A* and *B*. (*D*) Plot of peak current normalized to maximum current. The mean data from six cells were well fit by a single Boltzmann function with the half-inactivation voltage (Vh) of −72 mV and slope of 14.9 mV. (*E*) Scatter plots (mean indicated by horizontal line) showing the slope and half-inactivation voltage (Vh) for the same six cells. (*F*) Summary data for the same six cells for the inactivation time constant, (*t*) as a function of voltage (taken from the activation protocol in Fig. 3). Data were fit by a single exponential.

(2 ms to 100 ms) whose amplitude was adjusted to evoke an AP on 50% of trials for a given duration pulse (Higgs and Spain 2011). This method allows attainment of spikes in response to different rates of depolarization and allowed us to measure the effect of blocking Kv2 channels on AP threshold, as well as threshold accommodation, AP time course, and the membrane voltage trajectories following an AP (Fig. 5A,B). Consistent with the activation of Kv2 current near AP threshold in *Thy1* neurons, block of Kv2 resulted in a 2–4 mV negative shift in the voltage for AP threshold (for the first spike in response to a depolarizing current pulse). This effect was evident for all durations of current injections but only reached statistical significance for the 10 and 25 ms steps ($P < 0.05$, two-tailed Student's *t*-test; Fig. 5). In contrast, GTx had only a minimal effect on spike threshold accommodation, defined as a change in threshold dependent on the rate of depolarization (i.e., in GTx, there was a parallel shift in voltage threshold as a function of duration of current injection; Fig. 5D, upper). This result differs from the strong contribution that Kv1 channels have on accommodation, presumably because of the more rapid activation kinetics of Kv1, as well as their dominant location near the spike initiation zone of the AIS compared with Kv2 (Kole et al. 2007; Ogawa et al. 2008; Higgs and Spain 2011).

Integrated rheobase was measured from the amplitude of the 100 ms current steps required to evoke an AP on ~50% of trials, multiplied by the time along the step when an AP first occurred (note APs often occurred before the end of the 100 ms current steps especially in GTx). Integrated rheobase was lower in GTx (mean ± SE = 31.3 ± 5.5 pA_*s in control solution vs. 24.8 ± 4.0 pA_*s in GTx, $n = 8$ cells, $P = 0.03$, two-tailed paired student's T-test). We found small but significant effects of 100 nM GTx on AP amplitude (112 ± 2.7 mV control vs. 107 ± 2.95 mV GTx, $n = 12$. $P < 0.02$), and the rates of depolarization (dV/dt for upstroke of AP: 480 ± 26.5 V/s control vs. 452 ± 24.8 V/s GTx, $n = 12$, $P < 0.04$) and repolarization (dV/dt for downstroke of AP: 480 ± 26.5 V/s control vs. 452 ± 24.8 V/s GTx, $n = 12$, $P < 0.04$). There was no

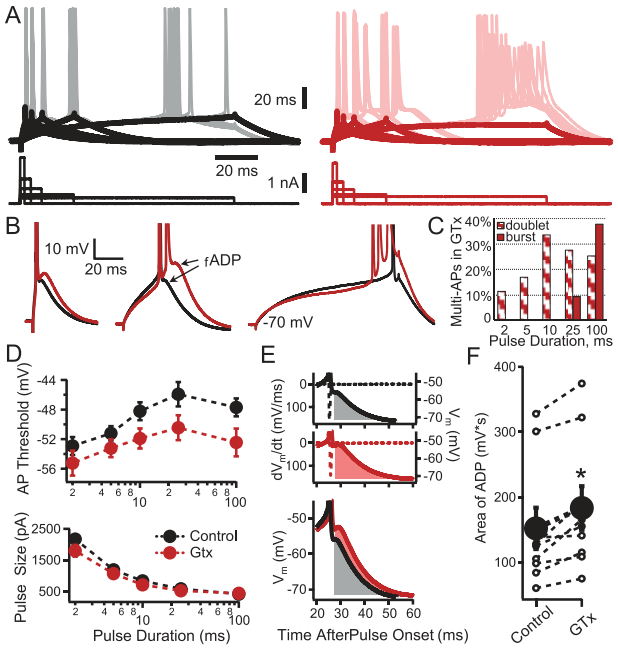

Figure 5. Effect of GTx on action potential threshold and the $_f$ADP. (*A*) Representative somatic whole-cell current-clamp recording of a *Thy1* PN in control (black, left) and in the presence of GTx 100 nM (red, right). Superimposed sweeps are shown of voltage responses (upper) evoked by current steps (lower) of varying duration (2, 5, 10, 25, and 100 ms). The amplitudes of the current steps were adjusted to elicit action potentials 50% of the time. The thick black and red lines denote the average voltage trajectory of nonspiking trials, which were used to facilitate measurement of spike threshold in traces when an AP was elicited. (*B*) Examples of suprathreshold voltage responses from 2, 25, and 100 ms current steps in control (black) and GTx (red). Note that GTx increases the size of the $_f$ADP and, in some cases, results in bursts of three or more APs. (*C*) Histogram showing the percent of cells that were converted in GTx to onset doublet or burst firing at each duration of current pulse. (*D*) The mean ± SEM for AP threshold (top) and current amplitude (bottom) is plotted as a function of the current step duration in control and GTx (black and red, respectively), $n = 9$. GTx caused a small decrease in AP threshold for all durations of current (significant for the 10- and 25-ms steps, $P < 0.05$, two-tailed Student's *t*-test). (*E*) Example of the method used for quantification of the effect of GTx on $_f$ADP size during 25-ms current steps for control and GTx conditions. Only trials with a single AP during the 25-ms current step were used. The membrane voltage (solid lines) and dV/dt (dotted lines) are plotted versus time after current-step onset. The $_f$ADP size was calculated as the integral (shaded areas) of the postspike voltage after crossing dV/dt = 0 until the return of the baseline membrane voltage (−70 mV). The bottom panel shows the control and GTx conditions superimposed. (*F*) Comparison of $_f$ADP size (integrals of area after the AP as in *D*) in control and GTx (individual cells = open circles; mean ± SEM = closed circles, $n = 9$ cells; $P < 0.0025$ Student's paired *t*-test).

significant difference for AP half-width (for the initial evoked AP measured at one half the amplitude from RMP to the peak AP) in control (0.75 ± 0.04 ms) versus GTx (0.77 ± 0.03 ms, $n = 12$ cells, $P < 0.13$).

In control bath solution, *Thy1* PNs respond to current injections with an initial single AP or a doublet (2 APs). As in the 2p-glu uncaging experiments, Kv2 block resulted in the conversion of the AP onset response to a burst of multiple spikes, especially for small and long current pulses that cause a shallow rise to the first AP. We define a burst as 3 or more APs generated at high frequency and arising from an $_f$ADP. Note that during such multispike bursts, the AP threshold becomes depolarized for APs subsequent to the first AP in the burst. The APs also become shorter and broader; thus, the depolarized voltage thresholds for APs occurring within the burst are likely due to accumulated inactivation of voltage-gated sodium channels. We found that under our recording conditions all neurons fired with a single AP at onset in control solution except for the 100 ms injections, where 1 of 9 responded with a doublet. In the presence of 100 nM GTx, onset firing was converted to doublet or burst firing in most cells when stimulated with a 100 ms pulse (Fig. 5B,C).

While the activation time constants measured from macropatches (~15 ms at membrane potential, *Vm*, near $_f$ADP occurrence and ~25 ms at −40 mV; Fig. 3E) are consistent with the minimal effect Kv2 block has on the AP waveform, Kv2 should activate rapidly enough to dampen the $_f$ADP following an AP. To examine this more closely, we measured the $_f$ADP as the integral of the area under the voltage trajectory following the AP until it crossed the resting potential and became an after-hyperpolarization ($_m$AHP; Fig. 5E). We found that GTx caused a consistent and significant increase in the amplitude and area of the $_f$ADP (amplitude: −51.3 mV ± 1.1 in control vs. -48.34 mV ±1.3 in GTx, $P < 0.0001$; area: 152 ± 31.8 mV∗ms in control vs. 183 ± 33.5 mV∗ms in GTx, $P < 0.0025$; n-9, Student's paired *t*-test).

Kv2 Conductance Limits both Onset and Repetitive Bursting in *Thy1* Neurons

The experiments of Figure 5 suggested that Kv2 channel current decreases the likelihood of an onset burst by opposing the $_f$ADP. Conversely, reducing Kv2 current facilitates onset bursting. Repetitive bursting after stimulus onset is rarely observed in neocortical PNs under normal conditions (but see Agmon and Connors 1992), but repetitive bursting in deep L5 PNs is an important factor associated with the initiation of cortical seizures (Connors 1984; Chagnac-Amitai and Connors 1989; Pinto et al. 2005; Traub et al. 2005). We therefore tested the effect of blocking Kv2 channels on onset and repetitive firing in response to long current steps.

A majority of *Thy1* PNs respond to DC current steps in control solution with an initial spike doublet or burst at the step onset that is followed by repetitive firing that does not adapt (e.g., Fig. 6A, black trace). As previously noted for motor cortex, most *Thy1* PNs show an increase in firing rate with time during DC steps (38 of 44 neurons in this study; this is referred to as warm-up firing: Miller et al. 2008). Figure 6A shows the typical effect of GTx on AP firing during long DC steps. GTx converted the initial AP doublet into a multispike burst riding on an enhanced $_f$ADP (i.e., an onset burst). In addition, GTx converted the sustained regular firing pattern evoked by a current step in this cell into repetitive bursts, with the interburst interval set by the duration of an enhanced $_m$AHP (see Fig. 8).

We quantified the effect of blocking Kv2 channels on onset firing by comparing the firing (spike) rate for the first three interspike intervals (ISIs) before and after GTx. This allowed us to test for the presence of onset singlet, doublet, or burst firing (APs within a burst or doublets are indicated by much higher spike rates (Hz: determined as 1/ISI) than subsequent APs: Fig. 6B,C). Under control conditions, the firing rate for the first ISI was higher at the onset of all current steps above 400 pA, indicating that it is normal for *Thy1* neurons to fire with an initial doublet (see also Guan et al. 2018). In GTx, firing rates for all three ISIs were higher (the instantaneous frequencies increased Fig. 6B,C) at all current intensities. In addition, at the lowest current steps, *GTx* converted onset single spiking to doublets and at 600 pA or greater, doublets into ≥3-spike bursts. Figure 6D summarizes the distribution of onset APs into singlets, doublets, or bursts

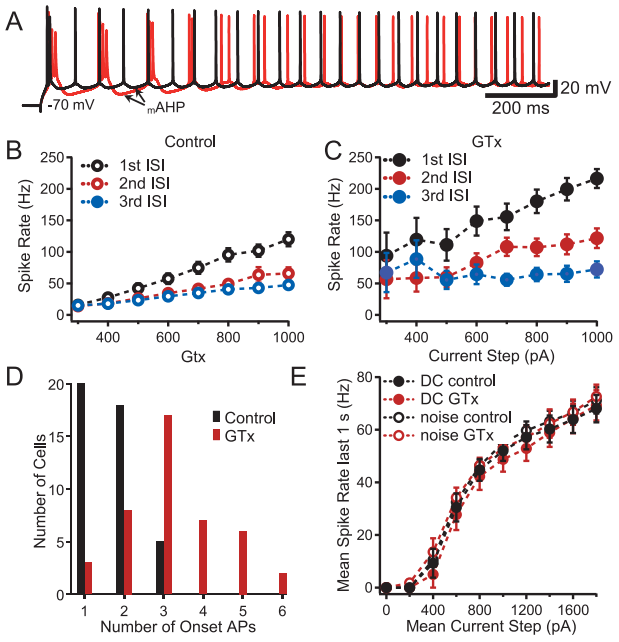

Figure 6. Effect of GTx on repetitive firing. (*A*) Superimposed voltage traces of AP firing in control (black) and GTx 100 nM (red) evoked by a long 600 pA current step from −70 mV. Note the enhanced duration and amplitude of the $_{m}$AHP following a burst of APs. (*B*, *C*). Firing rates (in Hz) for the initial three interspike intervals (ISIs) evoked by long current steps plotted as a function of the current step amplitude in control (*B*) and in GTx (*C*), ($n = 23$, error bars = SEM). The spike rate is calculated from 1/ISI for each of the first three ISIs. (*D*) Histogram of number of onset short-interval APs (i.e., single-onset APs, doublets, or bursts) before (control) and after GTx. Each cell was counted once in the column representing the most onset APs seen at any level of DC current ≤1.8 nA ($n = 43$). (*E*) Plot of AP firing frequency as a function of the mean current step amplitude for DC-only steps and DC plus noise steps (exponentially filtered noise, $\tau = 5$ ms: the amplitude of the noise current fluctuation was set to give a 2 mV standard deviation of membrane potential when the mean *Vm* was maintained at −70 mV). Spike rate was calculated for the final second of a 3-s current step (i.e., after repetitive bursting had stopped). DC current only, filled circles; DC current plus noise, open *circles*; control, *black*; GTx, red; $n = 4$.

in control bath and in GTx. After application of GTx, most *Thy1* neurons had an initial three-spike burst (especially for larger current steps, not shown). These data highlight the important role of Kv2 channels in regulating the onset burst firing pattern. It should be noted that bursting in PNs can be enhanced at lower extracellular calcium concentrations both in the slice and in vivo (Su et al. 2001; Boucetta et al. 2013). Our slice experiments were performed using extracellular calcium concentration (2 mM) that may be higher than those estimated in cerebrospinal fluid (1.1–1.5 mM: Jones and Keep 1988; Massimini and Amzica 2001; Crochet et al. 2005; Forsberg et al. 2019). Thus, it is possible that our ex vivo measurements might underestimate the role of Kv2 in controlling bursting in vivo.

Repetitive bursting was identified by visual inspection as the presence of two or more bursts during a current step (i.e., at least one burst after the onset burst). GTx caused repetitive bursting for at least one level of DC current injection in ~40% of *Thy1* PNs (20 of 51 cells). We also tested the firing of 15 *etv1* PNs in response to GTx, as an example of an L5 IT-type PN (Groh et al. 2010; Guan et al. 2013; Bishop et al. 2015) (data not shown). In contrast to the ET-type *Thy1* PNs, *etv1* PNs rarely showed repetitive bursting after Kv2 block. While all of the cells were able to fire with an initial doublet in response to higher current injections (cf. Guan et al. 2018), none of the 15 *etv1* cells fired with onset or repetitive bursts in control solution. In GTx, only 3 of 15 cells fired with an onset burst (20%) and none of them fired with repetitive bursts.

During constant current steps, GTx-induced repetitive bursting typically only lasted for the first half second of the step and then firing returned to a regular pattern. Plots of firing frequency at the end of long current steps (i.e., when there was no bursting: from 2 s to 3 s after stimulus onset) versus mean injected current (*F-I* relationship) showed that GTx caused very little change in firing rate to any current (Fig. 6*E*). This was also true when the *F-I* relationship was analyzed for the time interval 500–1000 ms after stimulus onset (data not shown). The lack of effect of GTx on the *F-I* relation in *Thy1* neurons contrasts with the decrease in firing rate caused by GTx previously reported as the dominant effect in CA1 (Du et al. 2000; Liu and Bean 2014), entorhinal cortex (Hönigsperger et al. 2017), and rat neocortical PNs from layers 2–3 and 5 (Guan et al. 2013). This decrease in firing rate was attributed to accumulated inactivation of voltage-dependent sodium channels secondary to depolarized interspike membrane voltage trajectories after block of Kv2 and suggests that Kv2 expression may be permissive for high rates of firing in PNs. The lack of a preferential decrease in firing to large stimuli after GTx in *Thy1* PNs is consistent with the hyperpolarized activation range for Kv2 channels in these cells making them available at all rates of firing. The overall lack of a significant effect of GTx on firing rate is consistent with inactivation of Na^+ channels not being a limiting factor for firing rate in *Thy1* PNs. As a test of this, we used stimuli including rapid current fluctuations that remove sodium channel inactivation and found that firing rates were insignificantly affected compared with DC steps in *Thy1* PNs under control conditions (Fig. 6*E*). The level of noise used in this example (see legend for Fig. 6*E*) induced an onset burst in the presence of GTx for all four cells tested (compared with none in control solution). Further, GTx had little effect on firing to noisy stimuli that did not cause repetitive bursting (2 mV SD noise response at RMP in Fig. 6*E*).

To rule out that repetitive bursting might have resulted from a partial block of Kv4-type channels by GTx, we tested the effect of the selective Kv4 blocker AmmTx3 (200 nM) on firing during 1.5 s long depolarizing current steps. No cells showed burst firing in control solutions for this sample of 13 *Thy1* PNs. In the presence of AmmTx3, we only observed an onset burst in 2/13 (15%) of *Thy1* PNs (the initial doublet firing was converted to a three-spike initial burst) and none of these cells showed repetitive bursting. Thus, the Kv2 current that is normally activated during firing is sufficient to suppress onset bursting and prevent repetitive bursting in *Thy1* neurons, even when Kv4 channels are blocked. Similarly, repetitive firing was tested in 20 cells before and in the presence of the selective Kv1 channel blocker 100 nM α-dendrotoxin (DTx). In control solution, 19 of 20 cells (95%) fired with an initial doublet followed by regular spiking (the remaining cell had an onset burst). In the presence of DTx, doublets were obtained in all cells with smaller stimuli and six cells (30%) showed an initial onset burst (no cells showed repetitive bursting). Thus, the block of Kv2 channels had a much more powerful effect on burst firing in *Thy1* PNs compared with block of Kv1 or Kv4 channels.

Repetitive Bursting Alters AP Firing Resonance to Low-Frequency Inputs

In order to determine the role of Kv2 channels in the regulation of bursting during more natural patterns of input, we evoked

repetitive firing in response to current steps composed of a DC level with added noisy current fluctuations (as used in Fig. 6E). The filtered noise has statistics similar to synaptic current fluctuations arriving at the soma of neocortical PNs, as previously measured from in vivo recordings in awake behaving animals (Pare et al. 1998). In previous work, we determined that layer 2/3 neocortical pyramidal neurons that fire with a regular spiking pattern to DC input will exhibit repetitive doublet firing when driven with rapid and large amplitude current fluctuations (we previously termed this "conditional bursting": Higgs and Spain 2011). Low-amplitude input fluctuations make the ISIs irregular but do not cause this repetitive doublet firing. Since we wanted to test the role of Kv2 channels in suppressing repetitive, multispike bursting during these more naturalistic fluctuating inputs, we first kept the amplitude of the fluctuations low (noise response at RMP = 2 mV SD) so as to prevent "conditional bursting" under control conditions.

In control solution, repetitive bursts were never seen in neurons driven with the low amplitude of noise we employed. In contrast, block of Kv2 channels with GTx resulted in repetitive bursting to noisy stimuli in 47% of *Thy1* neurons (8 of 17 cells). Figure 7A shows a typical trace of a *Thy1* PN in which GTx resulted in repetitive bursting during the naturalistic (noisy) current injection. Note that unlike the response to DC steps without noise (where repetitive bursting only lasted for the first few hundred milliseconds of the current step), the bursts in response to noisy stimuli persisted throughout the 10-s stimulus (Fig. 7A,B). Injecting higher amplitude noise (noise that caused 6 mV SD at RMP) in control conditions was capable of driving repetitive doublets (not bursts), and GTx application increased the occurrence of both repetitive doublets and bursts (data not shown). As previously noted, following each burst, there was an enhanced $_{m}$AHP that limited and regularized the rate of repetitive bursting (quantified in Fig. 8B). Thus, Kv2 channels normally suppress sustained repetitive bursting during natural patterns of somatic current input.

We previously showed for layer 2/3 PNs (Higgs and Spain 2009) that the relative efficacy of the various frequency components of a noisy stimulus to modulate firing rate can be calculated and represented as a gain–frequency relation and we refer to the frequency components that most robustly modulate AP firing as the suprathreshold resonance frequency. We employed this strategy to calculate the suprathreshold resonance of *Thy1* neurons under control and GTx conditions, while keeping the mean firing rate constant at ~20 Hz (a midrange firing rate during activity of PNs in motor cortex) by adjusting the DC level of the current steps while maintaining a constant standard deviation of the amplitude of the noisy component of the current (Fig. 7).

Figure 7C (black circles) shows that in control solutions, ISIs in *Thy1* PNs were distributed with a single peak at ~50 ms (20 Hz) with short ISIs related to doublets or bursts rarely occurring. In regular spiking neurons, the frequency components of the input current that most strongly drive AP output are typically matched to the mean firing frequency of the neuron. Thus, when driving the neurons to a mean firing rate of 20 Hz under control conditions, we unsurprisingly observed a maximal gain centered at 20 Hz (Fig. 7D). As we have described previously in other PNs, *Thy1* neurons also exhibit another peak in the gain–frequency relation at much higher frequency (~300 Hz) that results from high-pass filtering caused by AP threshold accommodation (Higgs and Spain 2011).

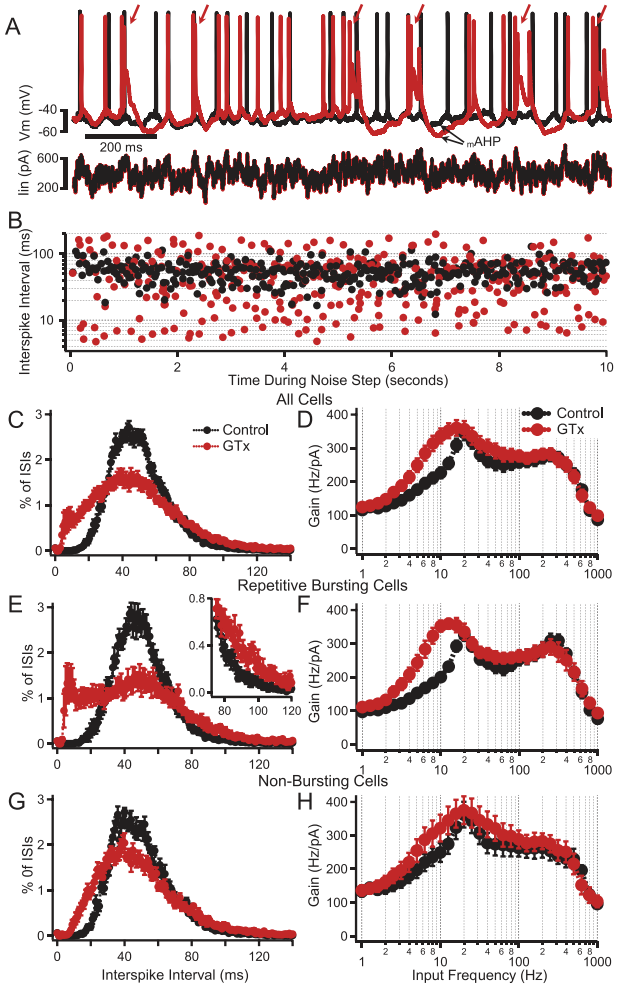

Figure 7. Effect of GTx on the frequency dependence of AP firing gain. (*A*) Superimposed voltage traces (upper) showing the initial AP firing response to a noise plus DC current step (lower) in control solution (black) and in GTx 100 nM (red). Mean firing rate during the 20-s step was maintained at 20 Hz by adjustment of the DC component of current injection. Note that in this neuron, GTx caused repetitive bursts of AP firing (arrows). (*B*) Semilog plots of ISI versus time (control and GTx) for the neuron shown in *A*. GTx caused at shift from a uniform distribution of ISIs centered around the mean firing rate (control, black) to a bimodal distribution with a subset of much shorter ISIs (GTx, red). (*C*) Normalized ISI histogram for all neurons receiving a 2 mV standard deviation noisy current input and driven to spike at 20 Hz with DC current injection in control (black) and GTx (red), $n = 17$. Error bars in *C*—*H* are mean ± SEM. (*D*) Plots of gain of AP firing as a function of frequency component of the input noise for the neurons in *C*. (*E*) Plots of ISI histograms as in *C* but for the subset of neurons that showed repetitive bursting in GTx ($n = 8$). Neurons were selected as repetitive busters (in GTx) if the ISI histogram showed a clear bimodal distribution of ISIs with a second peak <20 ms. Note the approximate doubling of the percent of 90 ms ISIs in GTx (inset). (*F*) Gain versus frequency plots for neurons showing repetitive bursting in GTx. (*G*) Plots of ISI histograms for the subset of neurons in which GTx did not cause repetitive bursting ($n = 9$). (*H*) Gain versus frequency plots for nonrepetitive bursting neurons.

Blocking Kv2 channels had two main effects that depended on whether GTx caused a substantial amount of repetitive bursting or a more uniform shift in the distribution of ISIs during the noise plus DC-induced firing (Fig. 7E vs. G). In PNs where the block of Kv2 channels resulted in sustained repetitive

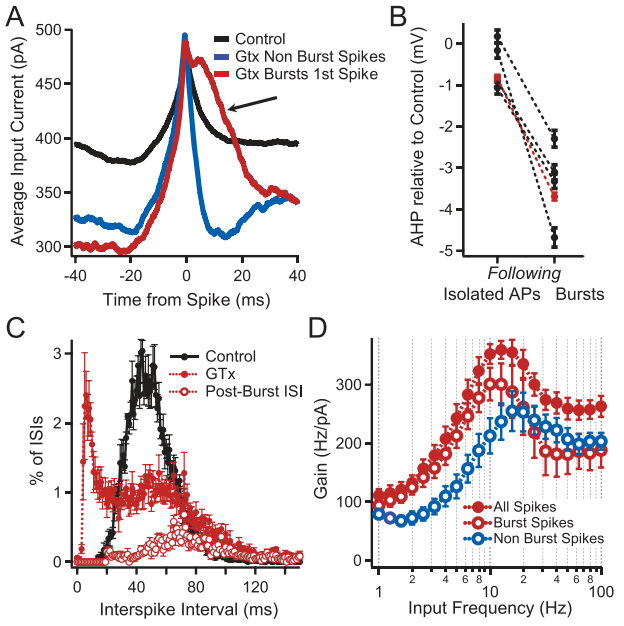

Figure 8. Effect of repetitive bursting on firing resonance. (*A*) Spike triggered average (STA) of the injected current that evoked APs from the subset of neurons in Figure 7*E* in which ≥40% of their APs were contained in bursts during noisy current injection ($n = 4$). STAs were determined from 1) all APs in the four neurons in control solution (black), 2) from APs not contained in bursts during GTx application (blue), and 3) from the first AP in a GTx-induced burst (red). Note the enhanced amplitude of the average stimulus current following the first AP contained in a burst (arrow). (*B*) Comparison of the mean $_{m}$AHP amplitude following isolated APs to the $_{m}$AHPs following bursts. Connected black circles represent values from the same cell. Red circles represent the mean of all $_{m}$AHP measurements from the four cells with mean ± SEM at −0.83 ± 0.08 mV following isolated spikes and −3.69 ± 0.09 mV following bursts (7563 $_{m}$AHPs after isolated APs vs. 4263 $_{m}$AHPs after bursts; $P < 0.001$ unpaired Student's *t*-test). Values are relative to the mean size of the $_{m}$AHPs from the same cell in control solution. (*C*) Plot of the ISI histograms for the four neurons of A in control (black) and GTx (red). Also plotted is the distribution of intervals between the end of a burst and the beginning of the next postburst AP (postburst ISI, open red circles). Error bars indicate SEM in *B*—*D*. Note that the postburst ISIs comprise the majority of the ISIs longer than 70 ms after GTx with mean = 89 ± 5.4 ms. (*D*) Superimposed plots of gain versus input frequency in GTx for the four neurons of A. The solid red circles show all APs for these cells. The open red circles show the subset of APs contained in bursts. The open blue circles indicate the subset of APs not contained in bursts. Note the peak gain shifts to a lower frequency for APs contained in bursts compared with APs not contained in bursts.

bursting (Fig. 7*E*), the distribution of ISIs has two peaks with a subset of very short ISIs and an increase in the number of very long ISIs (Fig. 7*E* inset). In these cells, the magnitude of the peak gain increased in GTx and peak gain frequency (or suprathreshold resonance frequency) shifted to a frequency less than the mean firing rate (Fig. 7*F*; from 21.45 to 12.7 Hz, $n = 9$, $P < 0.0002$). Thus, Kv2 normally prevents the entrainment of firing to low-frequency inputs (of ~10 Hz) that result from repetitive bursting.

For the subset of neurons where GTx did not cause substantial repetitive bursting (as determined by visual inspection and a lack of a clear peak or shoulder at short intervals in the ISI histogram; Fig. 7*G*,*H*), there was no significant change in the amplitude of the peak gain or the frequency at which peak gain occurred ($n = 8$). Rather, there was broadening of the sensitivity to input frequencies around the peak of gain versus frequency. Thus, block of Kv2 channels enhances the sensitivity of all *Thy1* PNs to low-frequency inputs and in a subset of cells, the transition to repetitive burst firing enhances the efficacy of input currents with frequency components well below the mean firing rate of the cell.

Repetitive Bursting Results in Firing Resonance to Theta Input Frequencies

The repetitive bursting group of PNs in Figure 7*E*,*F* includes neurons that had 12–52% of APs contained in bursts during 10-s noisy current steps. In order to gain insight into how repetitive bursting results and suprathreshold resonance is caused by the block of Kv2 channels, we further analyzed a subset of *Thy1* PNs in which GTx application resulted in greater than 40% of the APs being contained in bursts during the noisy current injection (four neurons from the group of busters in Fig. 7*E* met this criterion). We first analyzed if there were particular input current waveforms that favored bursting by comparing the STA of the input current for 1) all APs in control solution, 2) isolated APs in GTx, and 3) the first AP in a burst (Fig. 8*A*). This analysis revealed that the peak current immediately prior to threshold was the same in all cases. In control, DC current was required to drive the neuron to fire at 20 Hz. In GTx, less DC current was required, and the average current trajectory had shorter rise-times prior to APs. This likely resulted from an increase in accumulated Na^+ channel inactivation that occurred during firing when Kv2 channels were blocked. Thus, a faster rising stimulus was required on average to activate sufficient Na^+ current to evoke an AP. Further, comparison of the average current trajectory in GTx leading to isolated APs or the first AP in a burst had similar rise-times but the average input current waveform that drove bursts had a prolonged depolarizing-current hump following the onset of the initial spike in a burst (positive current hump indicated by arrow in Fig. 8*A*). The hump was absent in the STA for isolated APs. Note that although the noisy stimulus had the same statistics in GTx and control solution, normally the $_{f}$ADP is sufficiently blunted by Kv2 conductance so that slow current envelopes do not drive repetitive bursting. This suggests that reduction of Kv2 current would make neurons more susceptible to bursting when driven by synaptic inputs that contain a slow component (e.g., from NMDA receptor activation).

Prior work has shown that Ca^{2+} entry during the AP leads to activation of SK-type potassium channels and that this conductance contributes to the $_{m}$AHP, a major factor controlling the refractory period between APs (Schwindt et al. 1988; Lorenzon and Foehring 1993; Pineda et al. 1998; Guan et al. 2015). Each epoch of a multispike burst greatly enhances the Ca^{2+}-dependent $_{m}$AHP, which in turn controls the interburst interval (see also Huang et al. 2018). We used the same four champion bursters to quantify the amplitude of the $_{m}$AHP following a burst compared with following isolated APs in GTx (Fig. 8*B*) and found a significantly enhanced $_{m}$AHP following bursts. Thus, repetitive bursting would be expected to occur at regular intervals (on average) as determined by an enhanced $_{m}$AHP that dominates refractoriness.

We then analyzed the ISI histograms of the same four champion burster cells for 1) all APs in control, 2) all APs in GTx, and 3) for the distribution of intervals between the end of a burst and the beginning of the next postburst AP (Fig. 8*C*). This analysis revealed that after GTx application there was an increase in the amount of the longest ISIs and the postburst ISIs comprise the majority of the ISIs longer than 70 ms. These long ISIs following bursts likely result from the postburst enhancement

of the $_{m}$AHP and this could favor resonant firing to modulations of input current that match the time course of the $_{m}$AHP (Fuhrmann et al. 2002; Higgs and Spain 2009, 2013). We found this to be the case, as seen by comparison of the gain versus input frequency plots for spikes contained in a burst versus isolated APs in GTx (Fig. 8D). The peak gain of the isolated APs remained at the mean firing rate (i.e., ~20 Hz), as was the case for all APs in neurons where GTx did not cause bursting (Fig. 6H). In contrast, the peak gain of the spikes contained within bursts shifted to ~10 Hz (i.e., away from the mean firing rate). The shift of peak gain to ~10 Hz is determined by the time course of the enhanced $_{m}$AHP that in turn sets the interburst intervals. These data provide key insight as to why bursting *Thy1* PNs exhibit a stronger suprathreshold resonance at lower frequencies (10 Hz in GTx compared with 20 Hz in control; Fig. 7F).

Repetitive Bursting Results from the Increase in the $_{f}$ADP but Not from a Change in AP Threshold

We have shown that GTx caused changes in AP voltage threshold and changes in the postspike $_{f}$ADP (Fig. 5), either of which could potentially underlie the increased burst firing caused by GTx. We therefore analyzed phase plots of AP firing for the same four most prominent repetitive busters to provide insight into the relative contribution to burst firing of these two effects of GTx (Fig. 9). The phase plots of APs in control conditions versus GTx (both the single APs and the APs contained within bursts) showed no significant change in the maximum rate of rise for isolated APs or the first AP in a burst in GTx (black control trace vs. all other traces). However, APs subsequent to the first AP in a burst show reduced AP amplitude and a slower rate of spike repolarization (various green traces in Fig. 9A). Additionally, we observed that in GTx, the $_{f}$ADP was enhanced following each AP contained in a burst, but not following nonburst APs or following control APs (Fig. 9B). This analysis also showed that there was no significant change in threshold for the first AP in a burst compared with control APs or nonburst APs in GTx (Fig. 9B). Unlike the effect of blocking Kv1 channels that control spike threshold accommodation (Higgs and Spain 2011), during Kv2 block, the variability of the voltage at which threshold occurs was unchanged between control and the first AP in a burst. Thus, both the phase plot and STA analysis (Fig. 8) reveal that the control of repetitive bursting by Kv2 conductance is mediated primarily via its interaction with the $_{f}$ADP and not by its relatively minor contribution to AP threshold.

A Simple Model Captures Kv2 Function in Thy1 Neurons

Burst firing in ET-type neocortical PNs has been shown to facilitate rhythmicity in cortical circuits (Timofeev et al. 2000; Traub et al. 2005; Wang 2010; Stark et al. 2013; Wilson 2014; Beatty et al. 2015; Song et al. 2016; Sakmann 2017) and we have shown above that Kv2 channels are the primary regulators of burst firing in ET-type PNs. Epilepsy can be considered a pathological extreme form of cortical rhythmicity. Defects in Kv2 channel function have been found to underlie epilepsy in human families (D'adamo et al. 2013) and mice (Speca et al. 2014; Hawkins et al. 2021) and burst firing in deep layer 5 PNs has been shown to drive neocortical epileptiform activity (Connors 1984; Chagnac-Amitai and Connors 1989; Pinto et al. 2005). We found that Kv2 block leads to onset burst firing in virtually all *Thy1* PNs and repetitive bursting in over 40% of them. We hypothesized that repetitive bursting in a subset of L5 PNs due to loss of Kv2 channel function could entrain the local neocortical circuit and lead to rhythmic seizure-like activity. We tested the feasibility of our hypothesis by constructing a model circuit in silico that contains a subset of Kv2-deficient *Thy1*-like neurons.

The inhibitory, *I*, neurons used for the circuit were constructed as simple leaky integrate and fire, LIF, neurons. The excitatory, *E*, neurons were constructed as LIF plus three additional conductances (g) to reproduce the key features we measured in the *Thy1* cells in this study: g_{fADP}, g_{mAHP}, and g_{Kv2}. Because our knowledge of the ion channel distribution and properties of L5 PNs is far from complete, we did not attempt to relate changes in conductance to the underlying biophysics, but instead consider a simplified description of the postspike voltage trajectories and Kv2 current's contribution to them with parameters chosen based on our experimental data (Fig. 10A and Higgs and Spain 2009). The g_{Kv2} was designed to reproduce the experimentally measured major portion of the postspike Kv2 current evoked when a previously recorded AP waveform (from a *Thy1* neuron), which included $_{f}$ADP and $_{m}$AHP, was used as the voltage-command during *Thy1* macropatch recordings ($n = 3$ PNs). We used the voltage waveforms from both control and GTx current-clamp recordings to experimentally measure the difference between evoked outward current in control and GTx (Fig. 10A). These recordings showed that Kv2 comprised almost all of the outward current during the $_{f}$ADP while contributing 50% or less of the outward current during the AP itself. The full set of equations and variables used for the *E* and *I* neurons and their synapses are provided in the Materials and Methods.

The model neuron parameters (Table 1) were adjusted so that they captured the key experimentally measured features of *Thy1* neurons when stimulated with DC inputs (Fig. 10B), or noisy current steps (Fig. 10C) and the effect of GTx on the experimentally measured gain versus frequency relations. Consistent with our experimental findings, when g_{Kv2} was turned off in the model *E* neurons, there was an enhanced $_{f}$ADP, repetitive bursting to long noisy current steps, the ISI histogram became bimodal (Fig. 10D), and an increase in the peak suprathreshold gain magnitude with a shift to a lower frequency than the mean firing rate (Fig. 10E; compare with Figs 4B, 6A, 7E, and 6F).

Block of Kv2 Channels in a Few Neurons Causes Theta Rhythmicity in a Circuit Model

We next used a sparsely connected circuit of the model neurons (see Materials and Methods), to test if the internal correlations that result from repetitive bursting (as occurs with block of Kv2 in *Thy1* neurons) could cause the circuit to oscillate rhythmically. The circuit contained 240 neurons (200 *E* and 40 *I*). Neurons were randomly connected with a 10% chance of any neuron synapsing on another in the circuit between (i.e., ~24 synapses onto each neuron, with autapses removed).

The circuit was activated by stimulating each neuron continuously with a 6-s noisy current step to mimic synaptic input in the awake state in vivo. The noisy current driving each neuron was uncorrelated. After 2 s, g_{Kv2} was turned off in a subset of the *E* neurons. Figure 11A shows a raster plot of firing for all 240 neurons in the circuit. Prior to turning off g_{Kv2}, there appeared to be some correlated firing across the neurons. This comes from the connectivity in the circuit because it is lost when the circuit is run without connections (Fig. 11B and gray trace in Fig. 10C). In the connected circuit, prior to g_{Kv2} shutoff, the power spectral analysis (PSD) of the population activity of the *E* neurons was

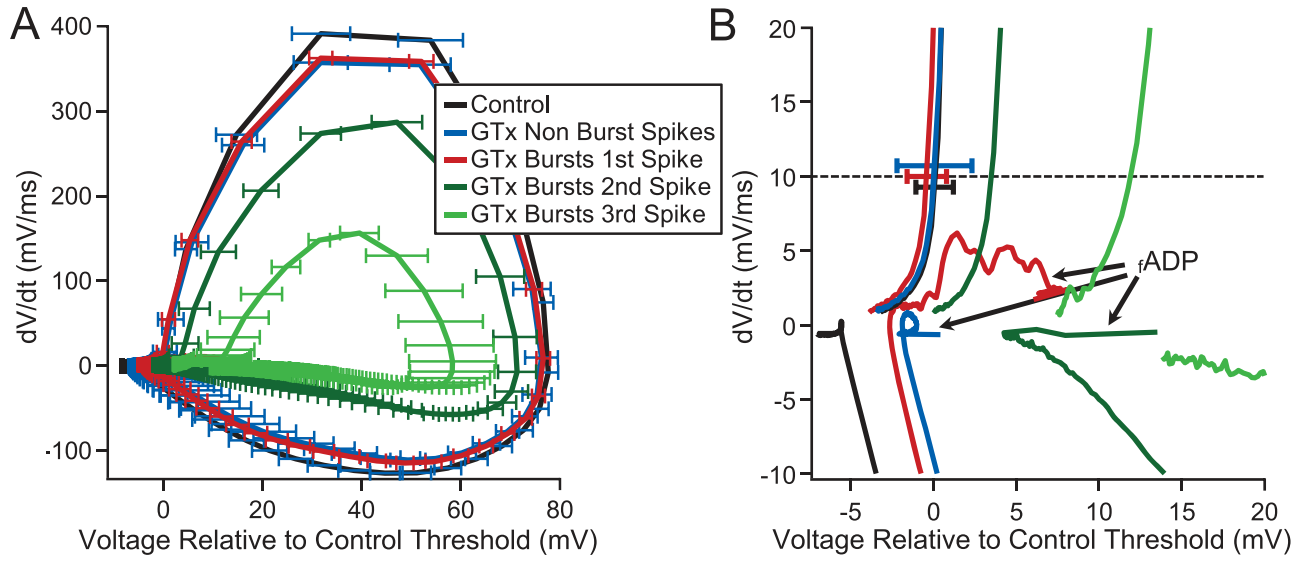

Figure 9. Analysis of AP threshold and the $_{f}$ADP during repetitive bursting. (A) Phase plots: first derivative of the time-dependent change of membrane potential (dV/dt) versus voltage (relative to AP threshold in control solution for each neuron, which was set to 0 mV). Data are from the same four cells used for Figure 8 (bars = standard deviation, SD). Individual phase plots are shown for control spiking (black), and spiking in GTx for nonburst APs (blue) and for the first, second, and third AP in bursts (red, dark green, and light green, respectively). (B) Expanded view of A showing the enhanced $_{f}$ADP following the APs contained in a burst compared with $_{f}$ADPs following nonburst APs or following control APs. Dotted line indicates dV/dt = 10 mV/ms, which was used for comparing the voltage of AP threshold between conditions. The error bars indicate the SD of threshold for the control APs (black), the nonburst APs in GTx (blue), and the first AP in a burst (red). There was a small but insignificant decrease in threshold for the first AP in a burst compared with control APs or nonburst APs in GTx (threshold was significantly increased for the second and third AP in a burst, caused by accumulated Na^+ channel inactivation, which occurs during high-frequency burst firing (Williams and Stuart 1999). Note the slower time course and smaller amplitude of the second and third AP in bursts. Note also that the variability of the voltage at which threshold occurs was essentially unchanged between control APs and the first AP in a burst (in GTx). The larger $_{m}$AHP after the burst APs is not shown over the plotted time range.

broadband with the peak power from cells 1–160 occurring at ~11 Hz (which was near their mean firing rate of 12.3 Hz; black trace in Fig. 11C). After g_{Kv2} is shutoff in 20% of the *E* neurons (neurons 161–140, red), the raster plot of all the neurons shows a dramatic increase in the correlated firing. Quantification of the change in correlation caused by shutoff of g_{Kv2} was assessed by comparing the PSD (from the *E* neurons in which g_{Kv2} remained intact) before and after shutoff of g_{Kv2}. The PSDs, after g_{Kv2} shutoff, shows a dramatic increase in the peak power that shifts to ~7.3 Hz (although the mean firing rate for *E* cells 1–160 was ~16 Hz; green and orange traces in Fig. 11C). The shift in peak power to ~7 Hz corresponds to the mean interburst interval in the Kv2-deficient neurons and the enhanced $_{m}$AHP following a burst suggests it may be the major intrinsic determinant of the interburst interval (Fuhrmann et al. 2002; Higgs and Spain 2009) and thus the entrainment of the circuit to theta frequency. This hypothesized role of the mAHP in determining the interburst interval requires further study that is beyond the scope of the present investigation.

The effect of changing the number of g_{Kv2}-deficient neurons in the circuit is shown in the PSD plots of a subset of *E* neurons in which g_{Kv2} always remains intact (cells 1–150; Fig. 11D). Note that as the number of neurons without g_{Kv2} is increased from 0 to 25% of *E* neurons, there is an increase in peak power with a gradual shift to lower frequencies (for 0, 10, 15, 20, or 25% g_{Kv2}-deficient *E* cells, the peak power in *E* cells 1–150 occurred at ~11.6, 9.7, 9.1, 6.9, or 6.7 Hz, respectively). These simulations show that repetitive bursting in a minority of Kv2-deficient neurons creates correlations that dominate the circuit firing activity, making it less responsive to the temporal information contained in external inputs (e.g., the noisy input to each neuron), similar to what happens in focal epilepsy.

Discussion

Our goal in this study was to test whether Kv2 channels play a role in regulating burst firing in a genetically distinct subset of ET-type PNs in neocortex (EYFP-expressing neurons from the *Thy1* mouse line). We found that Kv2.1 channels underlie a key potassium conductance that regulates burst firing in these cells. We showed that reduction of this conductance facilitates onset bursts and results in repetitive burst firing in response to naturalistic, noisy inputs. Furthermore, when this conductance is reduced in only a small percentage of neurons in a model local circuit, this can entrain network activity to have seizure-like rhythmic activity.

The Unique Role of Kv2 in Thy1 PNs

We found that in *Thy1* PNs, the GTx-sensitive (putative Kv2) current is the largest component of outward current in somatic macropatches and has biophysical properties that are consistent with a role in regulating the $_{f}$ADP and burst firing. GTx was selective for the sustained, delayed rectifier component of the outward current, with <10% block of the fast, transient A-type current (Herrington et al. 2006; Liu and Bean 2014; Bishop et al. 2015; Hönigsperger et al. 2017). Similar to Kv2 current in other PNs (Murakoshi and Trimmer 1999; Guan, Armstrong, et al. 2007a; Guan, Horton, et al. 2011b; Liu and Bean 2014; Bishop et al. 2015), GTx-sensitive currents activate rapidly (but slower than Kv1- or Kv4-mediated currents in PNs: Guan et al. 2006; Guan, Armstrong, et al. 2007a; Guan, Lee, et al. 2007b; Norris and Nerbonne 2010) and inactivate slowly (see also Hönigsperger et al. 2017). Those activation kinetics are too slow to strongly affect the AP waveform but fast enough to affect the initial post-AP membrane potential trajectory (e.g., the $_{f}$ADP).

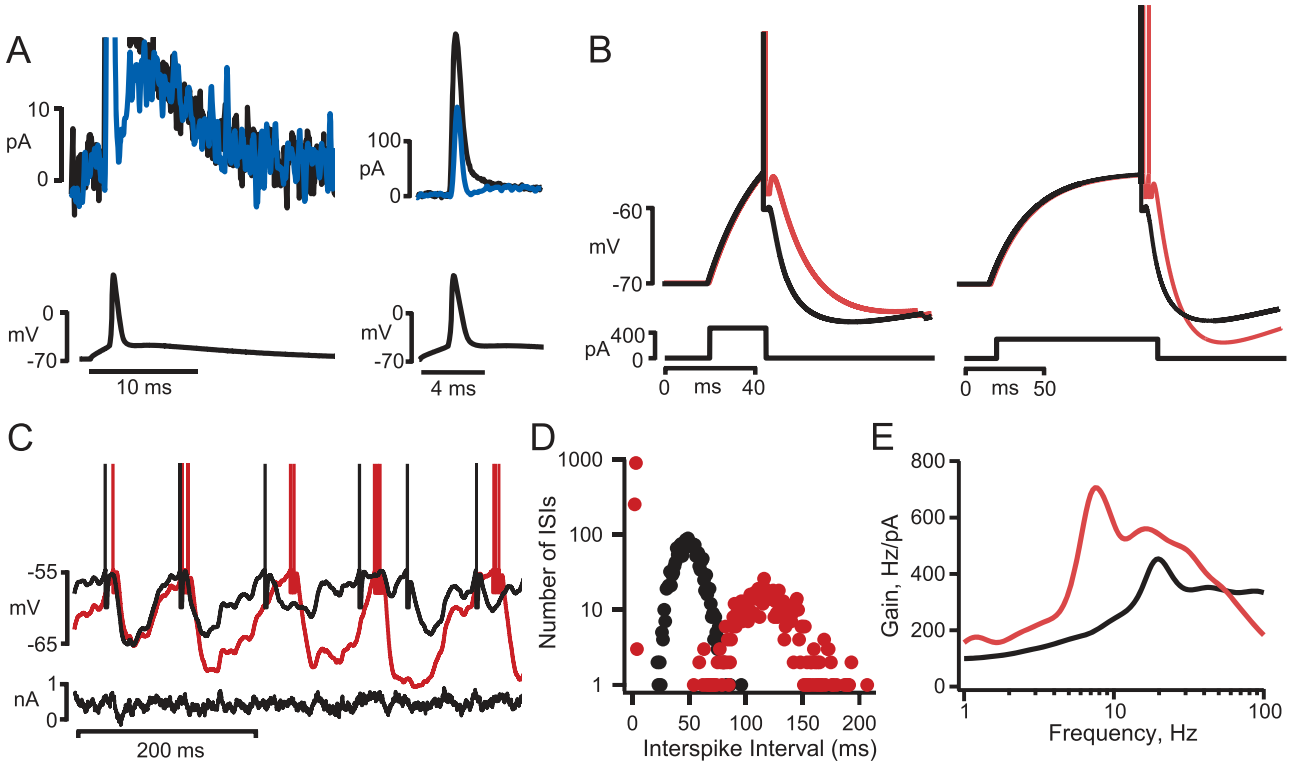

Figure 10. Implementation of a simplified model neuron that captures Kv2 channel control of bursting in *Thy1* neurons. (*A*) Average current (upper traces) obtained from outside-out macropatches pulled from the soma of three *Thy1* neurons. The voltage command (lower traces) was a previously recorded action potential evoked by 2-ms pulses (from a previous whole-cell recording from the soma of a *Thy1* neuron as in Figure 5). The total evoked K^+-current in control solution (black) is superimposed on the difference current after GTx application (blue is control minus GTx, i.e., the current attributable to Kv2 channels, average from three neurons). While Kv2 current accounted for less than half of the total K current during the AP, it accounted for essentially all of the K^+ current during the $_f$AHP (The bath included 0.5 μM TTX and 400 μM Cd^{2+} to block voltage-gated Na^+ and Ca^{2+} channels, respectively). (*B*) Voltage response of the model neuron to depolarizing current pulses with (black) and without Kv2-like conductance (red). (*C*) Voltage response of the model neuron to a noisy current step with (black) and without Kv2-like conductance (red). (*D*) ISI histogram (note that the *y*-axis is plotted on a log scale) for the model neuron during a 10-s noisy current step (black, with Kv2 conductance, red, without Kv2). The mean firing rate was maintained at ~20 Hz by adjusting the DC level of the current step (665 pA with Kv2; 450 pA without Kv2, the standard deviation of the noise was 200 pA in both cases). (*E*) Plot of firing gain as a function of input frequency for the model neuron responses used for *D*.

In contrast to Kv2 current in ET-type *glt25* PNs but similar to IT-type *etv1* PNs, activation voltage-dependence was hyperpolarized in *Thy1* PNs (half activation voltage was ~−27 mV for *Thy1* vs. ~−24 mV for *etv1* and~−13 mV for *glt25*: Bishop et al. 2015). The negative activation range may be due to different mechanisms in *etv1* PNs (which express Kv2.1 and Kv2.2: Bishop et al. 2015) and *Thy1* (which do not express Kv2.2). One possible source of these differences is expression of nonconducting auxiliary Kv subunits, which are known to associate with Kv2 subunits and alter their biophysical properties (Bocksteins and Snyders 2012; Bocksteins 2016).

Our experiments suggest that a major function of Kv2.1 channels in *Thy1* PNs is to prevent runaway bursting. The dominant effect of Kv2 block reported in other neuron types is that Kv2 blockade results in decreased firing in response to large currents preferentially due to the inactivation of Na^+ channels by sustained depolarization during the ISIs (Du et al. 2000; Guan et al. 2013; Liu and Bean 2014; Hönigsperger et al. 2017). We saw no significant effect of GTx on nonbursting repetitive firing in *Thy1* PNs, consistent with the possibility that Na^+ channels are less prone to inactivation during ISIs in these cells. Perhaps this is related to *Thy1* PNs responding reliably to phasic inputs with onset burst firing and their ability to maintain a steady or even increasing output (warm-up firing: Miller et al. 2008) in response to tonic synaptic activation. An alternative possibility is that Kv2.1 channels are largely inactivated before the time period analyzed (2–3 s after step onset). The similar lack of effect observed at 500–1000 ms after step onset argues against this. The inactivation time constant at voltages similar to those traversed by ISIs during repetitive firing is around 500 ms (see Fig. 4), suggesting it would be inactivated before 2 s; however, comparison of the steady-state activation and inactivation curves (Figs 3 and 4, respectively) shows a substantial window current between −70 and + 20 mV, suggesting that channels are active and not inactivated at steady state. Further study is needed to determine why sustained high-frequency firing is preserved in *Thy1* PNs after Kv2 block.

Kv2 block by GTx also leads to bursting in a few other neuron types, including entorhinal cortex neurons (Hönigsperger et al. 2017), dissociated dopamine neurons from substantia nigra (Kimm et al. 2015), and CA3 PNs (Raus Balind et al. 2019). Bursting in these other neuron types was distinct from what we observed in *Thy1* PNs, however. No repetitive bursting to tonic stimuli was reported in dopamine and CA3 neurons. In entorhinal cortical neurons, repetitive bursting was sometimes observed but only during small depolarizing current steps. The mechanism(s) underlying these differences could derive from the subunit composition and/or the cellular distribution of these channels. In the

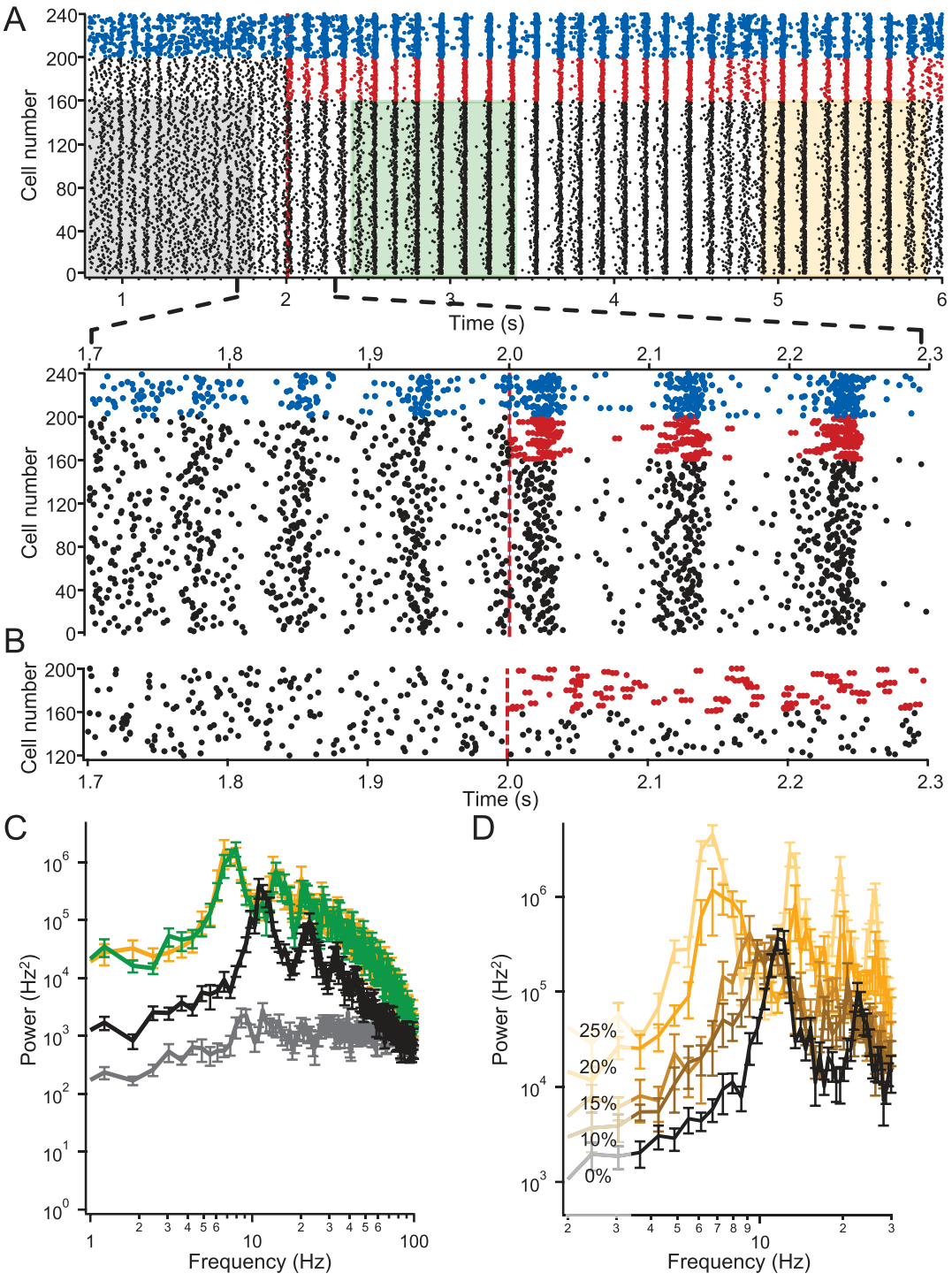

Figure 11. Effect of Kv2 block on rhythmicity in a subset of neurons in a simplified model of a local cortical circuit (full details in Materials and Methods and text). (*A*) Top: Raster plot of firing of 200 excitatory neurons (*E*; black, with Kv2 or red without Kv2) and 40 inhibitory (*I*, blue) neurons in a randomly connected circuit (10% chance of synaptic connection). Each neuron was driven by a random seed of exponentially filtered noise (i.e., uncorrelated noise to each neuron with tau = 5 ms and standard deviation = 350 pA) with a 350 pA DC offset for *E* neurons or a 125 pA DC offset for *I* neurons. Note that Kv2 is turned off after 2 s (red dashed line) of firing in 40 *E* neurons (color change from black to red). Shaded areas indicate 1-s epochs of firing where the power density plots of corresponding color in *C* were calculated. Bottom: The raster is shown at an expanded time base around the time when Kv2 is turned off. (*B*) Same as A except the neurons are not connected. (*C*) Plots of the average power spectral density of firing for *E* neurons 1 through 160 (i.e., neurons in which Kv2 is always on) for runs from 10 different 10% randomly connected circuits for a 1-s time period prior to tuning Kv2 off in a different set of *E* neurons in the circuit (black), 400 ms after turning off Kv2 (green) and 2.9 s after turning off Kv2 (orange). Gray trace is for the same set of neurons but from 10 runs of unconnected circuits. (*D*) Plots of the power spectral density of firing for *E* neurons 1 through 150 (i.e., Kv2 always on) after Kv2 is tuned off in 10% (dark brown), 15% (light brown), 20% (orange), or 25% (yellow) of the 200 *E* neurons (2.9 s after Kv2 turned off; avg. from 10 different circuit runs with 10% connectivity). Black PSD plot is from same set of 150 *E* neurons prior to turn off of Kv2.

CA3 PNs, GTx increased the likelihood of bursting emanating from a calcium spike in the tuft region of the apical dendrite, and Kv2.2 had a greater role in controlling bursting than Kv2.1. Similar to other neocortical PN subtypes (Trimmer 1991; Misonou et al. 2005; Guan, Armstrong, et al. 2007a; Guan et al. 2013; Sarmiere et al. 2008; Bishop et al. 2015), *Thy1* PNs express Kv2.1 channels on the soma and proximal dendrites (within ~50 μm of the soma). Furthermore, *Thy1* PNs do not express Kv2.2 channels, similar to the ET-type *glt25* PNs but unlike the IT-type *etv1* PNs (Bishop et al. 2015).

Associated with changes in bursting in *Thy1* PNs, Kv2 channels also profoundly shaped which input frequencies these neurons preferred to respond to. With Kv2 channels intact, firing of *Thy1* PNs was not particularly sensitive to noisy stimuli compared with IT-like neurons (*etv1*), consistent with the much reduced slow afterhyperpolarization ($_s$AHP) in *Thy1* PNs (the amplitude of the $_s$AHP is correlated with the degree of gain enhancement caused by noisy stimuli: Higgs et al. 2006). After Kv2 block, the sensitivity of all *Thy1* PNs to low-frequency inputs was enhanced, and in the subset of *Thy1* PNs where Kv2 block caused repetitive burst firing, there was also entrainment of firing to low-frequency inputs (of ~10 Hz). This entrainment is a form of suprathreshold resonance (Higgs and Spain 2009).

While our experiments examined complete block of Kv2 channels with GTx, effects on Kv2 function in PNs in response to transmitters, ischemia, or general anesthesia may also alter cortical function (including circuit rhythmicity). Numerous signaling pathways are known to modulate the expression pattern (clustering), current amplitude, and biophysics of Kv2.1 channels by changes in phosphorylation state (Misonou et al. 2005). Ca^{2+}-dependent dephosphorylation of Kv2.1 by calcineurin shifts steady-state activation to more hyperpolarized potentials and declusters the channels (Misonou et al. 2004, 2005, 2006). Large increases in neuronal activity also lead to dephosphorylation of Kv2.1, resulting in graded changes in its voltage-dependent activation, causing channels to activate at more hyperpolarized membrane potentials and homeostatic suppression of neuronal excitability (Surmeier and Foehring 2004; Mohapatra et al. 2009). The same pathway can also be activated by ischemia, glutamate, or CO_2 (Misonou et al. 2005). In CA1 PNs, muscarinic receptor activation causes a dephosphorylation-dependent left shift in steady-state activation for Kv2.1 channels (Mohapatra and Trimmer 2006) through activation of PLC and an IP_3-dependent increase in intracellular Ca^{2+}. Conversely, anesthesia with pentobarbital enhanced phosphorylation of Kv2.1 channels in rat brains (Missonou et al. 2006) and general anesthetics (propofol, halothane, and ketamine) reduce Kv2-mediated current in neocortical PNS (Kulkarni et al. 1996; Zhang et al. 2016). Given our finding that Kv2 channels prevent burst firing, it is notable that anesthetics elicit burst firing in ET but not IT PNs (Christophe et al. 2005).

Functional Implications of Kv2 Control of Burst Firing

Our results suggest that Kv2 channels play a powerful regulatory role in a subset of layer 5 PNs that have an intrinsic capacity to fire in bursts. The functional importance of burst firing is incompletely known, but Lisman (1997) proposed that this firing pattern plays a unique role in cortical information processing compared with regular spiking. Burst firing may be important for coincidence detection by ensuring release of neurotransmitter when signals from single spikes may be filtered out (Lisman 1997; Williams and Stuart 1999). As such, burst firing can also code for the magnitude of input slope in a graded manner (Williams and Stuart 1999; Kepecs and Lisman 2003). However, these mechanisms are only likely to come into play when neocortical PNs are driven by phasic or fluctuating inputs and would not be expected to affect downstream tonic activity in neocortical circuits.

In addition to contributing to information processing in the neocortex, burst firing may also be crucial for initiation of cortical rhythmicity (Sakmann 2017). Correlated, rhythmic cortical activity may underlie cognition (Engel and Singer 2001; Singer and Lazar 2016), attention (Fries et al. 2001; Siegel et al. 2008; Womelsdorf et al. 2014; Sacchet et al. 2015), and perception (Rodriguez et al. 1999) and these rhythms can be impaired in disease (e.g., epilepsy and schizophrenia: McCormick and Contreras 2001; Uhlhaas and Singer 2010). In vivo recordings and computational models show that network rhythmicity can depend upon circuitry and synaptic dynamics (McCormick and Contreras 2001; Stark et al. 2013), and intrinsic neuronal properties (including the ability to fire in bursts: Pockberger 1991; Nunez et al. 1993; Timofeev et al. 2000; Traub et al. 2005; Wang 2010; Stark et al. 2013; Wilson 2014; Beatty et al. 2015; Song et al. 2016). We report here that changes in the internal dynamics of *Thy1* firing caused by Kv2 block could potentially have profound influence on the rhythmic activity of the cortical network in which these PNs are embedded. Our in silico model suggests that removal of a Kv2-like conductance in 5–10% of the *Thy1*-like neurons in the circuit resulted in the entrainment of firing of all neurons in the circuit to low frequencies (7–11 Hz).

The potential entrainment of neocortical circuits to rhythmic activity by a subset of repetitively bursting PNs is of clinical interest because it suggests a mechanism for pathological bursting in neocortex, which occurs in some forms of epilepsy. Deep layer 5 PNs (including the Thy1 PN cell type) have been shown to initiate and propagate neocortical epileptiform activity (Connors 1984; Wong et al. 1986; Silva et al. 1991; Telfeian and Connors 1998; Traub et al. 1999, 2005; Pinto et al. 2005; but see Timofeev et al. 2000). As might be expected from our findings, alterations in potassium channel expression or their properties can lead to neurological disorders including many different forms of epilepsy (Villa and Combi 2016). For example, it has been known that mutations in KNCB1, the gene that encodes for Kv2.1, can cause severe encephalopathies where symptoms typically exhibit in late infancy with generalized tonic–clonic seizures combined with delayed motor development. (Srivastava et al. 2014; Torkamani et al. 2014; Saitsu et al. 2015; Thiffault et al. 2015; Allen et al. 2016; Latypova et al. 2017; Kang et al. 2019). Motor abnormalities include increased involuntary movement of the upper limbs and stereotyped handwringing movements along with feeding difficulty. When these mutated human KNCB1 genes are expressed into *Neuro2a* cells (Saitsu et al. 2015), the cells showed inability to fire at high frequencies and a decreased action potential threshold, as we have reported here. Another human epilepsy was found to result from a mutation of the Kv8.2 subunit that arose from the altered activity of heteromeric Kv2.1/mutant Kv8.2 channels. (Jorge et al. 2011; D'Adamo et al. 2013) We hypothesize that these seizures may arise from decreased activity of Kv2.1 channels that convert ET-type PNs to burst mode firing.

Supplementary Material

Supplementary material is available at *Cerebral Cortex* online.

Funding

National Institute of Neurological Disorders and Stroke at the National Institutes of Health (R01 NS44163-14 to W.J.S. and R.C.F.).

Notes

We thank Mark Hudson for providing technical support and Yoni Browning and Brian Kim for help writing code in MATLAB used for the in silico model. Special thanks go to Dr Brent Doiron (University of Chicago) for reviewing the cortical circuit model and our analyses of it. *Conflict of Interest*: None declared.

References

Abel HJ, Lee JC, Callaway JC, Foehring RC. 2004. Relationships between intracellular calcium and afterhyperpolarizations in neocortical pyramidal neurons. *J Neurophysiol*. 91(1):324–335.

Agmon A, Connors BW. 1992. Correlation between intrinsic firing patterns and thalamocortical synaptic responses of neurons in mouse barrel cortex. *J Neurosci*. 12:319–329.

Allen NM, Conroy J, Shahwan A, Lynch B, Correa RG, Pena SDJ, McCreary D, Magalhães TR, Ennis S, Lynch SA, et al. 2016. Unexplained early onset epileptic encephalopathy: exome screening and phenotype expansion. *Epilepsia*. 57(1):e12–e17.

Anderson CT, Sheets PL, Kiritani T, Shepherd GM. 2010. Sublayer-specific microcircuits of corticospinal and corticostriatal neurons in motor cortex. *Nat Neurosci*. 13(6):739–744.

Baker A, Kalmbach B, Morishima M, Kim J, Juavinett A, Li N, Dembrow N. 2018. Specialized subpopulations of deep-layer pyramidal neurons in the neocortex: bridging cellular properties to functional consequences. *J Neurosci*. 38:5441–5455.

Beatty JA, Song SC, Wilson CJ. 2015. Cell-type-specific resonances shape the responses of striatal neurons to synaptic input. *J Neurophysiol*. 113(3):688–700.

Bekkers JM. 2000. Distribution and activation of voltage-gated potassium channels in cell-attached and outside-out patches from large layer 5 cortical pyramidal neurons of the rat. *J Physiol (Lond)*. 525:611–620.

Bishop H, Guan D, Bocksteins E, Parajuli L, Murray K, Cobb M, Misonou H, Zito K, Foehring R, Trimmer J. 2015. Distinct cell- and layer-specific expression patterns and independent regulation of Kv2 channel subtypes in cortical pyramidal neurons. *J Neurosci*. 35:14922–14942.

Bocksteins E. 2016. Kv5, Kv6, Kv8, and Kv9 subunits: no simple silent bystanders. *J Gen Physiol*. 47(2):105–125.

Bocksteins E, Snyders DJ. 2012. Electrically silent Kv subunits: their molecular and functional characteristics. *J Physiol (Lond)*. 27:73–84.

Boucetta S, Crochet S, Chauvette S, Seigneur J, Timofeev I. 2013. Extracellular Ca^{2+} fluctuations *in vivo* affect afterhyperpolarization potential and modify firing patterns of neocortical neurons. *Exp Neurol*. 245:5–14.

Brown SP, Hestrin S. 2009. Intracortical circuits of pyramidal neurons reflect their long-range axonal targets. *Nature*. 457:1133–1136.

Chagnac-Amitai Y, Connors BW. 1989. Synchronized excitation and inhibition driven by intrinsically bursting neurons in neocortex. *J Neurophysiol*. 62:1149–1162.

Chagnac-Amitai Y, Luhmann HJ, Prince DA. 1990. Burst generating and regular spiking layer 5 pyramidal neurons of rat neocortex have different morphological features. *J Comp Neurol*. 296:598–613.

Christophe E, Doerflinger N, Lavery DJ, Molnár Z, Charpak S, Audinat E. 2005. Two populations of layer V pyramidal cells of the mouse neocortex: development and sensitivity to anesthetics. *J Neurophysiol*. 94:3357–3367.

Connors BW. 1984. Initiation of synchronized neuronal bursting in neocortex. *Nature*. 310:685–687.

Connors BW, Gutnick MJ, Prince DA. 1982. Electrophysiological properties of neocortical neurons *in vitro*. *J Neurophysiol*. 8:1302–1320.

Crochet S, Chauvette S, Boucetta S, Timofeev I. 2005. Modulation of synaptic transmission in neocortex by network activities. *Eur J Neurosci*. 21(4):1030–1044.

D'Adamo MC, Catacuzzeno L, DiGiovanni G, Franciolini F, Pessia M. 2013. *K*+ Channelepsy: progress in the neurobiology of potassium channels and epilepsy. *Front Cell Neurosci*. 7:134.

Debanne D. 2011. The nodal origin of intrinsic bursting. *Neuron*. 71(4):569–570.

de Kock CP, Bruno RM, Spors H, Sakmann B. 2007. Layer- and cell-type-specific suprathreshold stimulus representation in rat primary somatosensory cortex. *J Physiol*. 581:139–154.

Dembrow NC, Chitwood RA, Johnston D. 2010. Projection-specific neuromodulation of medial prefrontal cortex neurons. *J Neurosci*. 30:16922–16937.

Du J, Haak LL, Phillips-Tansey E, Russell JT, McBain CJ. 2000. Frequency-dependent regulation of rat hippocampal somato-dendritic excitability by the K+ channel subunit Kv2.1. *J Physiol*. 522:19–31.

Engel AK, Singer W. 2001. Temporal binding and the neural correlates of sensory awareness. *Trends Cogn Sci*. 5(1): 16–25.

Feng G, Mellor RH, Bernstein M, Keller-Peck C, Nguyen QT, Wallace M, Nerbonne JM, Lichtman JW, Sanes JR. 2000. Imaging neuronal subsets in transgenic mice expressing multiple spectral variants of GFP. *Neuron*. 28:41–51.

Foehring RC, Surmeier DJ. 1993. Voltage-gated potassium currents in acutely-dissociated rat neocortical neurons. *J Neurophysiol*. 70:51–63.

Forsberg M, Seth H, Björefeldt A, Lyckenvik T, Andersson M, Wasling P, Zetterberg H, Hanse E. 2019. Ionized calcium in human cerebrospinal fluid and its influence on intrinsic and synaptic excitability of hippocampal pyramidal neurons in the rat. *J Neurochem*. 149(4):452–470.

Fries P, Reynolds JH, Rorie AE, Desimone R. 2001. Modulation of oscillatory neuronal synchronization by selective visual attention. *Science*. 291:1560–1563.

Fuhrmann G, Markram H, Tsodyks M. 2002. Spike frequency adaptation and neocortical rhythms. *J Neurophysiol*. 88:761–770.

Groh A, Meyer HS, Schmidt EF, Heintz N, Sakmann B, Krieger P. 2010. Cell-type specific properties of pyramidal neurons in neocortex underlying a layout that is modifiable depending on the cortical area. *Cereb Cortex*. 20:826–836.

Guan D, Armstrong WE, Foehring RC. 2015. Electrophysiological properties of genetically identified subtypes of layer 5 neocortical pyramidal neurons: Ca^{2+} dependence and differential modulation by norepinephrine. *J Neurophysiol*. 113:2014–2032.

Guan D, Armstrong WE, Foehring RC. 2007a. Kv2 subunits underlie slowly inactivating potassium current in rat neocortical pyramidal neurons. *J Physiol*. 581:941–960.

Guan D, Armstrong WE, Foehring RC. 2013. Kv2.1 channels regulate firing rate in pyramidal neurons from rat sensorimotor cortex. *J Physiol (Lond)*. 591:4807–4825.

Guan D, Higgs MH, Horton LR, Spain WJ, Foehring RC. 2011a. Contributions of Kv7-mediated potassium current to sub- and suprathreshold responses of rat layer II/III neocortical pyramidal neurons. *J Neurophysiol*. 106:1722–1733.

Guan D, Horton LR, Armstrong WA, Foehring RC. 2011b. Postnatal development of A-type and Kv1- and Kv2-mediated potassium channel currents in neocortical pyramidal neurons. *J Neurophysiol*. 105:2976–2988.

Guan D, Lee JC-F, Higgs M, Spain WJ, Armstrong WE, Foehring RC. 2007b. Functional roles of Kv1 channels in neocortical pyramidal neurons. *J Neurophysiol*. 97:1931–1940.

Guan D, Lee JCF, Tkatch T, Armstrong WE, Surmeier DJ, Foehring RC. 2006. Expression and biophysical properties of Kv1 channels in neocortical pyramidal neurons. *J Physiol (Lond)*. 571:371–389.

Guan D, Pathak D, Foehring RC. 2018. Functional roles of Kv1-mediated currents in genetically identified subtypes of pyramidal neurons in layer 5 of mouse somatosensory cortex. *J Neurophysiol*. 120(2):394–408.

Guatteo E, Franceschetti S, Bacci A, Avanzini G, Wanke E. 1996. A TTX-sensitive conductance underlying burst firing in isolated pyramidal neurons from rat neocortex. *Brain Res*. 741:1–12.

Hattox AM, Nelson SB. 2007. Layer V neurons in mouse cortex projecting to different targets have distinct physiological properties. *J Neurophysiol*. 98:3330–3340.

Hawkins NA, Misra SN, Jurado M, Kang SK, Vierra NC, Nguyen K, Wren L, George AL, Trimmer JS, Kearney JA. 2021. Epilepsy and neurobehavioral abnormalities in mice with a dominant-negative KCNB1 pathogenic variant. *Neurobiol Dis*. 147:105141.

Herrington J, Zhou YP, Bugianesi RM, Dulski PM, Feng Y, Warren VA, Smith MM, Kohler MG, Garsky VM, Sanchez M, et al. 2006. Blockers of the delayed-rectifier potassium current in pancreatic beta-cells enhance glucose-dependent insulin secretion. *Diabetes*. 55(4):1034–1042.

Higgs MH, Slee SJ, Spain WJ. 2006. Diversity of gain modulation by noise in neocortical neurons: regulation by the slow afterhyperpolarization conductance. *J Neurosci*. 26:8787–8799.

Higgs MH, Spain WJ. 2009. Conditional bursting enhances resonant firing in neocortical layer 2-3 pyramidal neurons. *J Neurosci*. 29:1285–1299.

Higgs MH, Spain WJ. 2011. Kv1 channels control spike threshold dynamics and spike timing in cortical pyramidal neurons. *J Physiol*. 589:5125–5142.

Higgs MH, Spain WJ. 2013. Neural encoding of dynamic inputs by spike timing. In: DiLorenzo PM, Victor JD, editors. *Frontiers in neuroscience; spike timing: mechanism and function*. Boca Raton, FL: CRC Press, Taylor and Francis Pub.

Hönigsperger C, Nigro MJ, Storm JF. 2017. Physiological roles of Kv2 channels in entorhinal cortex layer II stellate cells revealed by Guangxitoxin-1E. *J Physiol*. 595(3):739–757.

Huang Y, Liu X, Wang G, Wang Y. 2018. SK channels participate in the formation of after burst hyperpolarization and partly inhibit the burst strength of epileptic ictal discharges. *Mol Med Rep*. 17(1):1762–1774.

Ji N, Magee JC, Betzig E. 2008. High-speed, low-photodamage nonlinear imaging using passive pulse splitters. *Nat Methods*. 5(2):197–202.

Jones HC, Keep RF. 1988. Brain fluid calcium concentration and response to acute hypercalcaemia during development in the rat. *J Physiol*. 402:579–593.

Jorge BS, Campbell CM, Miller AR, Rutter ED, Gurnett CA, Vanoye CG, Kearney JA. 2011. Voltage-gated potassium channel KCNV2 (Kv8.2) contributes to epilepsy susceptibility. *Proc Natl Acad Sci USA*. 108(13):5443–5448.

Kang SK, Vanoye CG, Misra SN, Echevarria DM, Calhoun JD, O'Connor JB, Fabre KL, McKnight D, Demmer L, Goldenberg P, et al. 2019. Spectrum of Kv2.1 dysfunction in KCNB1-associated neurodevelopmental disorders. *Ann Neurol*. 86(6):899–912.

Kepecs A, Lisman J. 2003. Information encoding and computation with spikes and bursts. *Network*. 14:103–118.

Kimm T, Khaliq ZM, Bean BP. 2015. Differential regulation of action potential shape and burst-frequency firing by BK and Kv2 channels in substantia Nigra dopaminergic neurons. *J Neurosci*. 35:16404–16417.

Kole MH. 2011. First node of Ranvier facilitates high-frequency burst encoding. *Neuron*. 71:671–682.

Kole MH, Letzkus JJ, Stuart GJ. 2007. Axon initial segment Kv1 channels control axonal action potential waveform and synaptic efficacy. *Neuron*. 55:633–647.

Korngreen A, Sakmann B. 2000. Voltage-gated K^+ channels in layer 5 neocortical pyramidal neurones from young rats: subtypes and gradients. *J Physiol (Lond)*. 525:621–639.

Kulkarni RS, Zorn LJ, Anantharam H, Bayley H, Treistman SN. 1996. Inhibitory effects of ketamine and halothane on recombinant potassium channels from mammalian brain. *Anesthesiology*. 84(4):900–909.

Larkman A, Mason A. 1990. Correlations between morphology and electrophysiology of pyramidal neurons in slices of rat visual cortex. I. Establishment of cell classes. *J Neurosci*. 10(5):1407–1414.

Larkum ME, Kaiser KM, Sakmann B. 1999. Calcium electrogenesis in distal apical dendrites of layer 5 pyramidal cells at a critical frequency of back-propagating action potentials. *Proc Natl Acad Sci USA*. 96:14600–14604.

Larkum ME, Waters J, Sakmann B, Helmchen F. 2007. Dendritic spikes in apical dendrites of neocortical layer 2/3 pyramidal neurons. *J Neurosci*. 27:8999–9008.

Larkum ME, Senn W, Lüscher HR. 2004. Top-down dendritic input increases the gain of layer 5 pyramidal neurons. *Cereb Cortex*. 14:1059–1070.

Latypova X, Matsumoto N, Vinceslas-Muller C, Bézieau S, Isidor B, Miyake N. 2017. Novel KCNB1 mutation associated with non-syndromic intellectual disability. *J Hum Genet*. 62(5):569–573.

Lisman JE. 1997. Bursts as a unit of neural information: making unreliable synapses reliable. *TINS*. 20:38–43.

Liu PW, Bean BP. 2014. Kv2 channel regulation of action potential repolarization and firing patterns in superior cervical ganglion neurons and hippocampal CA1 pyramidal neurons. *J Neurosci*. 34:4991–5002.

Lorenzon NM, Foehring RC. 1992. Relationship between repetitive firing and afterhyperpolarizations in human neocortical neurons. *J Neurophysiol*. 67(2):350–363.

Lorenzon NM, Foehring RC. 1993. The ontogeny of repetitive firing and its modulation by norepinephrine in rat neocortical neurons. *Brain Res Dev Brain Res*. 73(2):213–223.

Maffie JK, Dvoretskova E, Bougis PE, Martin-Eauclaire MF, Rudy B. 2013. Dipeptidyl-peptidase-like-proteins confer high sensitivity to the scorpion toxin AmmTX3 to Kv4-mediated A-type K^+ channels. *J Physiol*. 591:2419–2427.

Marx M, Günter RH, Hucko W, Radnikow G, Feldmeyer D. 2012. Improved biocytin labeling and neuronal 3D reconstruction. *Nat Protoc*. 7(2):394–407.

Mason A, Larkman A. 1990. Correlations between morphology and electrophysiology of pyramidal neurons in slices of rat visual cortex. II. Electrophysiology. *J Neurosci*. 10:1415–1428.

Massimini M, Amzica F. 2001. Extracellular calcium fluctuations and intracellular potentials in the cortex during the slow sleep oscillation. *J Neurophsiol*. 85(3):1346–1350.

McCormick DA, Connors BW, Lighthall JW, Prince DA. 1985. Comparative electrophysiology of pyramidal and sparsely spiny stellate neurons of the neocortex. *J Neurophysiol*. 54:782–806.

McCormick DA, Contreras D. 2001. On the cellular and network bases of epileptic seizures. *Ann Rev Neurosci*. 63:815–846.

Miller MN, Okaty BW, Nelson SB. 2008. Region-specific spike-frequency acceleration in layer 5 pyramidal neurons mediated by Kv1 subunits. *J Neurosci*. 28:13716–13726.

Misonou H, Mohapatra DP, Park EW, Leung V, Zhen D, Misonou K, Anderson AE, Trimmer JS. 2004. Regulation of ion channel localization and phosphorylation by neuronal activity. *Nat Neurosci*. 7:711–718.

Misonou H, Mohapatra DP, Trimmer JS. 2005. Kv2.1: a voltage-gated K^+ channel critical to dynamic control of neuronal excitability. *Neurotoxicology*. 26:743–752.

Misonou H, Menegola M, Mohapatra DP, Guy LK, Park KS, Trimmer JS. 2006. Bidirectional activity-dependent regulation of neuronal ion channel phosphorylation. *J Neurosci*. 26:13505–13514.

Mohapatra DP, Misonou H, Pan SJ, Joshua E, Held JE, Surmeier DJ, Trimmer JS. 2009. Regulation of intrinsic excitability in hippocampal neurons by activity-dependent modulation of the KV2.1 potassium channel. *Channels (Austin)*. 3(1): 46–56.

Mohapatra DP, Trimmer JS. 2006. The Kv2.1 C terminus can autonomously transfer Kv2.1-like phosphorylation-dependent localization, voltage-dependent gating, and muscarinic modulation to diverse Kv channels. *J Neurosci*. 26:685–695.

Murakoshi H, Trimmer JS. 1999. Identification of the Kv2.1 K^+ channel as a major component of the delayed rectifier K^+ current in rat hippocampal neurons. *J Neurosci*. 19: 1728–1735.

Norris AJ, Nerbonne JM. 2010. Molecular dissection of I(A) in cortical pyramidal neurons reveals three distinct components encoded by Kv4.2, Kv4.3, and Kv1.4 alpha subunits. *J Neurosci*. 30:5092–5101.

Nunez A, Amzica F, Steriade M. 1993. Electrophysiology of cat association cortical cells *in vivo*: intrinsic properties and synaptic responses. *J Neurophysiol*. 70:418–430.

Oakley JC, Schwindt PC, Crill WE. 2001a. Initiation and propagation of regenerative Ca(2+)-dependent potentials in dendrites of layer 5 pyramidal neurons. *J Neurophysiol*. 86(1):503–513.

Oakley JC, Schwindt PC, Crill WE. 2001b. Dendritic calcium spikes in layer 5 pyramidal neurons amplify and limit transmission of ligand-gated dendritic current to soma. *J Neurophysiol*. 86(1):514–527.

Ogawa Y, Horresh I, Trimmer JS, Bredt DS, Peles E, Rasband MN. 2008. Postsynaptic density-93 clusters Kv1 channels at axon initial segments independently of Caspr2. *J Neurosci*. 28:5731–5739.

Pare D, Shink E, Gaudreau H, Destexhe A, Lang EJ. 1998. Impact of spontaneous synaptic activity on the resting properties of cat neocortical pyramidal neurons *in vivo*. *J Neurophysiol*. 79:1450–1460.

Pathak D, Guan D, Foehring RC. 2016. Roles of specific potassium conductances in repolarization of the action potential in genetically-identified subtypes of pyramidal cells in mouse neocortex. *J Neurophysiol*. 115:2317–2329.

Pineda JC, Galarraga E, Foehring RC. 1999. Different Ca2+ source for slow AHP in completely adapting and repetitive firing pyramidal neurons. *Neuroreport*. 10(9):1951–1956.

Pineda JC, Waters RS, Foehring RC. 1998. Specificity in the interaction of HVA Ca^{2+} channel types with Ca^{2+}–dependent AHPs and firing behavior in neocortical pyramidal neurons. *J Neurophysiol*. 79(5):2522–2534.

Pinto DJ, Patrick SL, Huang WC, Connors BW. 2005. Initiation, propagation, and termination of epileptiform activity in rodent neocortex in vitro involve distinct mechanisms. *J Neurosci*. 25:8131–8140.

Pockberger H. 1991. Electrophysiological and morphological properties of rat motor cortex neurons *in vivo*. *Brain Res*. 539:181–190.

Raus Balind S, Mago A, Ahmadi M, Kis N, Varga-Nemeth Z, Lorincz A, Makara JK. 2019. Diverse synaptic and dendritic mechanisms of complex spike burst generation in hippocampal CA3 pyramidal cells. *Nat Commun*. 10(1):1859.

Reiner A, Hart NM, Lei W, Deng Y. 2010. Corticostriatal projection neurons - dichotomous types and dichotomous functions. *Front Neuroanat*. 4:142.

Reiner A, Jiao Y, Del Mar N, Laverghetta AV, Lei WL. 2003. Differential morphology of pyramidal tract-type and intratelencephalically projecting-type corticostriatal neurons and their intrastriatal terminals in rats. *J Comp Neurol*. 457:420–440.

Rodriguez E, George N, Lachaux JP, Martinerie J, Renault B, Varela FJ. 1999. Perception's shadow: long-distance synchronization of human brain activity. *Nature*. 397:430–433.

Sacchet MD, LaPlante RA, Wan Q, Pritchett DL, Lee AKC, Hämäläinen M, Moore C, Kerr CE, Jones SR. 2015. Attention drives synchronization of alpha and Beta rhythms between right inferior frontal and primary sensory neocortex. *J Neurosci*. 35:2074–2082.

Saitsu H, Akita T, Tohyama J, Goldberg-Stern H, Kobayashi Y, Cohen R, Kato M, Ohba C, Miyatake S, Tsurusaki Y, et al. 2015. De novo KCNB1 mutations in infantile epilepsy inhibit repetitive neuronal firing. *Sci Rep*. 5:15199.

Sakmann B. 2017. From single cells and single columns to cortical networks: dendritic excitability, coincidence detection and synaptic transmission in brain slices and brains. *Exp Physiol*. 102(5):489–521.

Sarmiere PD, Weigle CM, Tamkun MM. 2008. The Kv2.1 K^+ channel targets to the axon initial segment of hippocampal and cortical neurons in culture and in situ. *BMC Neurosci*. 9:112.

Schmidt EF, Warner-Schmidt JL, Otopalik BG, Pickett SB, Greengard P, Heintz N. 2012. Identification of the cortical neurons that mediate antidepressant responses. *Cell*. 149:1152–1163.

Schwindt PC, Spain WJ, Foehring RC, Chubb MC, Crill WE. 1988. Slow conductances in neurons from cat sensorimotor cortex *in vitro*: their modulation by neurotransmitters and their role in slow excitability changes. *J Neurophysiol*. 59:450–467.

Siegel M, Donner TH, Oostenveld R, Fries P, Engel AK. 2008. Neuronal synchronization along the dorsal visual pathway reflects the focus of attention. *Neuron*. 60:709–719.

Silva LR, Amitai Y, Connors BW. 1991. Intrinsic oscillations of neocortex generated by layer 5 pyramidal neurons. *Science*. 251:432–435.

Singer W, Lazar A. 2016. Does the cerebral cortex exploit high-dimensional, non-linear dynamics for information processing? *Front Comput Neurosci*. 10:99.

Song SC, Beatty JA, Wilson CJ. 2016. The ionic mechanism of membrane potential oscillations and membrane resonance in striatal LTS interneurons. *J Neurophysiol*. 116(4): 1752–1764.

Speca DJ, Ogata G, Mandikian D, Bishop HI, Wiler SW, Eum K, Wenzel HJ, Doisy ET, Matt L, Campi KL, et al. 2014. Deletion of the Kv2.1 delayed rectifier potassium channel leads to neuronal and behavioral hyperexcitability. *Genes Brain Behav*. 13:394–408.

Srivastava S, Cohen JS, Vernon H, Barañano K, McClellan R, Jamal L, Fatemi A. 2014. Clinical whole exome sequencing in child neurology practice. *Ann Neurol*. 76(4):473–483.

Stark E, Eichler R, Roux L, Fujisawa S, Rotstein HG, Buzsáki G. 2013. Inhibition-induced theta resonance in cortical circuits. *Neuron*. 80(5):1263–1276.

Su H, Alroy G, Kirson ED, Yaari Y. 2001. Extracellular calcium modulates persistent sodium current-dependent burst-firing in hippocampal pyramidal neurons. *J Neurosci*. 21(12):4173–4182.

Surmeier DJ, Foehring RC. 2004. A mechanism for homeostatic plasticity. *Nat Neurosci*. 7:691–692.

Suter BA, Migliore M, Shepherd GM. 2013. Intrinsic electrophysiology of mouse corticospinal neurons: a class-specific triad of spike-related properties. *Cereb Cortex*. 23: 1965–1977.

Telfeian AE, Connors BW. 1998. Layer-specific pathways for the horizontal propagation of epileptiform discharges in neocortex. *Epilepsia*. 39:700–708.

Telfeian AE, Connors BW. 2003. Widely integrative properties of layer 5 pyramidal cells support a role for processing of extralaminar synaptic inputs in rat neocortex. *Neurosci Lett*. 343:121–124.

Thiffault I, Speca DJ, Austin DC, Cobb MM, Eum KS, Safina NP, Grote L, Farrow EG, Miller N, Soden S, et al. 2015. A novel epileptic encephalopathy mutation in *KCNB1* disrupts Kv2.1 ion selectivity, expression, and localization. *J Gen Physiol*. 146(5):399–410.

Timofeev I, Grenier F, Steriade M. 2000. Impact of intrinsic properties and synaptic factors on the activity of neocortical networks *in vivo*. *J Physiol Paris*. 94:343–355.

Torkamani A, Bersell K, Jorge BS, Bjork RL, Friedman JR, Bloss CS, Kearney JA. 2014. De novo KCNB1 mutations in epileptic encephalopathy. *Ann Neurol*. 76(4):529–540.

Traub RD, Contreras D, Whittington MA. 2005. Combined experimental/simulation studies of cellular and network mechanisms of epileptogenesis *in vitro* and *in vivo*. *J Clin Neurophysiol*. 22:330–342.

Traub RD, Jefferys JG, Whittington MA. 1999. Functionally relevant and functionally disruptive (epileptic) synchronized oscillations in brain slices. *Adv Neurol*. 79:709–724.

Trimmer JS. 1991. Immunological identification and characterization of a delayed rectifier K^+ channel polypeptide in rat brain. *Proc Natl Acad Sci USA*. 88:10764–10768.

Tseng GF, Prince DA. 1993. Heterogeneity of rat corticospinal neurons. *J Comp Neurol*. 335:92–108.

Uhlhaas PJ, Singer W. 2010. Abnormal neural oscillations and synchrony in schizophrenia. *Nat Rev Neurosci*. 11(2):100–113.

Villa C, Combi R. 2016. Potassium channels and human epileptic phenotypes: an updated overview. *Front Cell Neurosci*. 10:81.

Wang XJ. 2010. Neurophysiological and computational principles of cortical rhythms in cognition. *Physiol Rev*. 90:1195–1268.

Williams SR, Stuart GJ. 1999. Mechanisms and consequences of action potential burst firing in rat neocortical pyramidal neurons. *J Physiol (Lond)*. 521:467–482.

Wilson CJ. 2014. The sensory striatum. *Neuron*. 83(5):999–1001.

Womelsdorf T, Ardid S, Overlong S, Valiant TA. 2014. Burst firing synchronizes prefrontal and anterior cingulate cortex during attentional control. *Curr Biol*. 24:2613–2621.

Wong RK, Traub RD, Miles R. 1986. Cellular basis of neuronal synchrony in epilepsy. *Adv Neurol*. 44:583–592.

Zhang YZ, Zhang R, Zeng XZ, Song CY. 2016. The inhibitory effect of propofol on Kv2.1 potassium channel in rat parietal cortical neurons. *Neurosci Lett*. 616:93–97.